Analyst

Accepted Manuscript

This article can be cited before page numbers have been issued, to do this please use: L. Veliz and F. Lagugné-Labarthet, *Analyst*, 2026, DOI: 10.1039/D6AN00476H.

View Article Online
DOI: 10.1039/D6AN00476H

ARTICLE

Frontiers in Raman Nano-diagnostics: SERS and TERS of Extracellular vesicles for Cancer Detection

Lorena Veliz[a] and François Lagugné-Labarthet[a]*

+Received 00th January 20xx,
Accepted 00th January 20xx

DOI: 10.1039/x0xx00000x

Efforts to create rapid, non-invasive, and reliable cancer diagnostics have increasingly focused on extracellular vesicles (EVs), nanoscale carriers of proteins, lipids, and nucleic acids that mirror the molecular state of their parent cells and mediate communication within the tumor microenvironment. Their complex composition and heterogeneity present however, significant challenges for analytical characterization. Raman spectroscopy, with its ability to probe molecular vibrations, has emerged as a possible technique for EV analysis. In this review, we highlight recent advances in Raman-based techniques, including conventional Raman, surface-enhanced Raman spectroscopy (SERS), tip-enhanced Raman spectroscopy (TERS), and emerging hybrid modalities where nanomaterials serve as critical platforms to amplify signals and resolve EV heterogeneity. We discuss how engineered nanostructures enable sensitive detection, molecular fingerprinting, and spatially resolved characterization of EVs. Integration with machine learning data analytics approaches further enhances classification accuracy across healthy, benign, and malignant samples, improving the accuracy and reliability of the spectroscopic investigation. Finally, we discuss translational prospects, including AFM-IR technologies that appear particularly well suited to the analysis of single EVs, enabling interrogation of both surface chemistry and internal cargo owing to the greater penetration depth of infrared radiation. In parallel, microfluidic platforms offer powerful solutions for the controlled delivery, sorting, and trapping of EVs within optical microscopy configurations. Collectively, the continued development and integration of these non-invasive analytical tools hold substantial promise for EV-based cancer diagnostics and open new avenues for biomarker discovery.

1. Introduction

Extracellular vesicles (EVs) were first observed in the 1940s while a group of scientists was investigating the clotting factor in blood samples, which required high-speed centrifugation processes to separate the bio-fractions.[1] Here, Chargaff et al.[2] isolated a specific fraction separated at 31,000 g that contained several proteins, as well as other small biological bodies, which was later recognized as the EV fraction. The presence of these nanovesicles was further confirmed in a variety of biofluids such as ascites, tissues, blood, and tumor biopsies. However, despite the importance of their bio-content, EVs' role was reduced to the release of cellular waste into the extracellular space.

It was not until 1996 that Raposo et al. revealed that EVs can induce the activity of antigen-specific T-cells, which play a key role in the immune system's response to eliminate viruses or even cancer cells.[3, 4] Later on, it was demonstrated that tumor-derived EVs not only contain important proteins but also nucleic acids, which can be transferred from one cell to another, promoting tumoral growth. These discoveries marked the beginning of an entire field devoted to the exploration of EVs and the understanding of EVs' ability to transfer specific genetic information.[5]

EVs are complex, membrane-bound nanoscale vesicles that have attracted the attention of the research community. These organelles contain different metabolites such as proteins, lipids, and nucleic acids, which show concentrations directly dependent on the type of cell. Currently, the field of EVs is very dynamic, with many research teams focusing on the design of new and rapid isolation methodologies, characterization and imaging of vesicles using transmission or scanning microscopy (TEM and SEM), and concomitant analysis of large datasets to classify the content of EVs. Although in the past they were considered just cellular debris without any relevance, EVs have opened a new window in cancer research as relevant biomarkers, with the anticipated goal of developing early diagnosis tools.[6, 7]

1.1 EVs Composition, Formation, and Delivery mechanism

The extracellular vesicles are classified into three types depending on size and vesicle's content.[8] The first ones are apoptotic bodies with 1 – 5 µm diameter which are released from an apoptotic cell into the plasma. These apoptotic bodies normally contain fragments of proteins, RNA, DNA, and cellular organelles. The second type of EVs are ectosomes (including microvesicles), resulting from plasma membrane budding. The ectosomes were known as cellular material contained in blood plasma and serum, playing an important role in blood coagulation due to their platelet origins. However, recent studies have demonstrated that ectosomes derived from cancer cells (oncosomes) actively participate in cell communication mechanisms. Ectosomes have a diameter between 0.1 to 1 µm, and their content is composed of cytosolic proteins, lipids, and mRNA. [9, 10] The third and smallest EVs are the exosomes, formed internally within the multicellular vesicles (MVEs). MVEs are large vesicular bodies that encapsulate intraluminal vesicles

[a] Department of Chemistry, Western University (The University of Western Ontario), 1151 Richmond Street, London, ON, N6A 5B7, Canada.
*E-mail: flagugne@uwo.ca

View Article Online
DOI: 10.1039/D5AN00476H

(ILVs), which are subsequently transported, fuse with the plasma membrane, and are released as exosomes. With diameters ranging from 30 to 150 nm, exosomes play a direct role in intercellular communication, containing information about specific surface markers, such as tetraspanins CD9 and CD63, lipids, and RNA fragments.[11, 12] It is also important to note that the 3 types of EV are not produced through the same pathway and subsequently do not contain identical information.

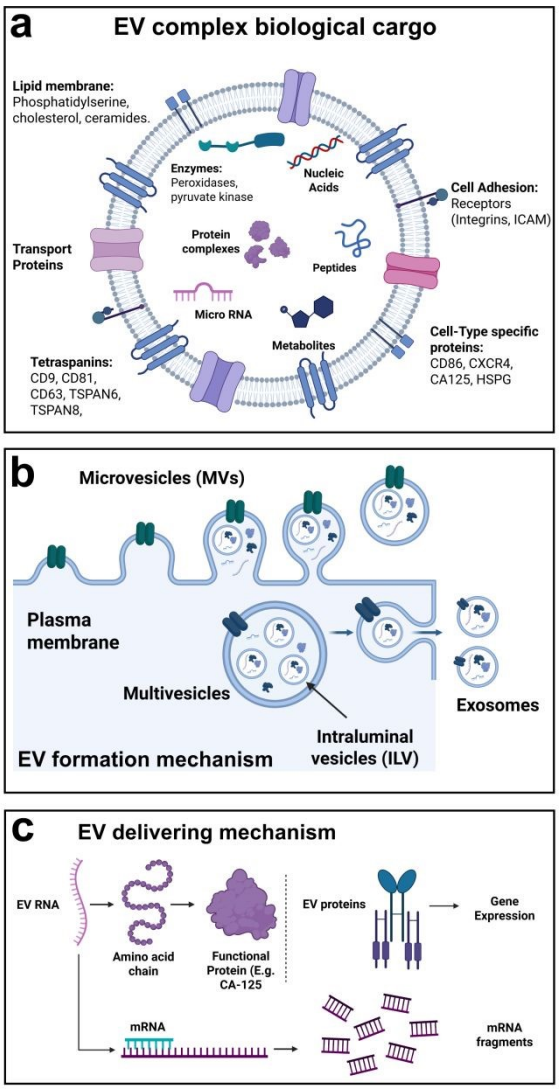

Figure 1. Summary of EV composition. b) The EV formation mechanism illustrates the two principal routes for producing microvesicles or exosomes. c) EVs serve as a delivery system for important information via EV proteins and RNA, allowing the production of specific functional proteins, influencing gene expression, and facilitating RNA degradation.

Aside from the size distribution and similar shape, compositional heterogeneity poses an obstacle when a comprehensive EV profile is required. Consequently, different EVs are challenging to detect and to classify, not only due to their size and the complex matrix in which these organelles exist, but also because of the variable composition based on their origin.[13] **Figure 1(a-c)** summarizes the composition, formation, and function of EVs, highlighting their roles in critical functions such as gene expression, the creation of functional proteins, and RNA degradation. In Addition, **Table 1** shows the common biomarkers, responsible for the basic EV functions, found in apoptotic bodies, ectosomes (microvesicles), and exosomes.

Table 1. Summary of basic biomarkers for the three main classes of EVs

Type	Biomarker	Ref.
Tetraspanins	CD9, CD63, CD81, CD83, CD154	14, 15
Cell-Adhesion (Integrins)	Integrin β3, αvβ1	12, 16
Lipid Membrane	Flotillin-1 and 2, cholesterol	8, 17
Heat shock proteins	HSP90, HSP70	18
Calcium-binding proteins	Annexin A1	19
Microvesicles proteins	ALIX, TSG101	9, 17, 20

1.2 Cancer-Derived EVs

The origins and spread of a tumor were initially considered to be a largely cell-autonomous process. It appears, however, that it is influenced by the communication of tumoral cells with their surroundings.[21] EVs are one of the many vectors by which cancer cells communicate with other cell types and the surrounding structures that constitute the tumor microenvironment (TME). The biogenesis of cancer-derived EVs is associated with several mechanisms that promote cancer development, migration, and invasion through healthy cells, modulation of the immune response, metastasis, and drug resistance.[22, 23] Numerous studies have examined the role of EVs in cancer progression, with one of the most significant being the transfer of bio-cargo enriched with cell surface receptors such as EGFRvIII (e.g., Glioblastoma), which can trigger tumor growth from aggressive glioma cells to healthy ones.[24] Also, EVs' cargo may contain indoleamine-2,3-dioxygenase, which stops T-cell proliferation, allowing tumor cells to evade detection and elimination by the immune system.[25, 26] Additionally, recent works suggest that the original content of the EV cargo may also significantly contribute to the understanding of EV proteomics, creating possibilities for exploring alternative therapeutic and diagnostic approaches.[27] As described, ectosomes and exosomes have an important influence on cancer progression. Thus, the disruption of communication via cancer-derived EV might result in a useful treatment strategy that can be achieved through the inhibition of exosome formation, release, or uptake by healthy recipient cells.

Despite advancements in the EV field and contributions from various scientists and groups, working with EVs remains a challenge due to their complex biology. Furthermore, researchers face a lack of standardized methods for the isolation, purification, and characterization of EVs. While suitable tools do exist, they come with limitations such as low EV concentration yield and heterogeneous subpopulation. Recent techniques have demonstrated the ability to isolate a purer fraction of EVs; however, specific biomarkers for these subpopulations, especially for early-stage cancer diseases, have

View Article Online
DOI: 10.1039/D6AN00476H

yet to be identified. **Table 2** summarizes several biomarkers for most of the common cancer diseases that are used for diagnostic purposes.

Table 2. Summary of principal biomarkers identified for the most common and lethal cancer diseases.

Type of cancer	Biomarker	Sample fluid	Ref.
Breast Cancer	HER2, CD9, CD63, PGR, miRNA-1246	Plasma	15, 28
	HER2, EpCAM, EGFR, CD44	Serum	29
Lung Cancer	miRNA-21, miRNA-451, CD63, TNC, VCAN	Plasma	30
	PD-1/PD-L1 mRNAs and PD-1/PD-L1 proteins	Serum	31
Colorectal Cancer	CD147, miRNA-139-3p, miRNA-145-3p, CD24	Plasma	32
	KRAS and BRAF mutation mRNA	Serum	15, 33
Cervical Cancer	miRNA-21, miRNA-221-3p, CD24	Serum	34
Prostate Cancer	miRNA-141	Serum	35
Ovarian Cancer	CD24, EpCAM	Plasma	36-38

1.3 Emerging Characterization Strategies for EV Profiling

Many efforts are currently being investigated for the development of new, rapid, and effective methods for cancer detection at the early stages of tumor growth. The most common protocols for cancer diagnosis are based on biopsies derived from the affected zone to directly analyze the tumor cells by a pathologist, making these methods invasive, time-consuming, and costly. As an alternative, the use of body fluids offers advantages due to the rapid and non-invasive collection of these samples. The specific collection and analysis of extracellular vesicles (EVs) that are secreted by all cells is indeed a promising venue and an important source of components to detect cancer markers effectively.

In general, the detection and characterization of extracellular vesicles are based on physical techniques such as transmission electron microscopy (TEM), scanning electron microscopy (SEM), atomic force microscopy (AFM), and dynamic light scattering (DLS).[39-41] These techniques are capable of physically detecting EVs due to their high spatial resolution and size quantification. Nonetheless, chemical characterization through these methods is not possible, and complementary studies based on biochemical techniques must be applied. Thus, the most common techniques used for elucidating the chemical profile of the EVs are: Immunoblotting techniques, Immunoassays (ELISA and LFIA), and mass spectrometry (MS). Nevertheless, the main disadvantages of these methods are low specificity and throughput, long preparation times, and high cost. [42] In this context, optical measurements can play an important role in yielding a precise biological mapping of EVs, thus enhancing early detection of cancer. Among them, Raman spectroscopy can provide sufficient sensitivity and spatial resolution to analyze and classify EVs subpopulation. Together with advanced numerical analysis, Raman spectroscopy and its surface-enhanced version are a viable alternative for EV molecular profiling in complex biofluids derived from cancer samples.

2. Raman Spectroscopy for Biological Samples

As we approach the 100th anniversary of C. V. Raman's discovery,[43] Raman spectroscopy has evolved far beyond its fundamental origins into a versatile analytical technique now widely applied in environmental science, biology, and the food sector. Its application in medicine is also widely investigated by leading research groups. Raman spectroscopy overcomes many limitations of other optical techniques by providing a molecularly specific vibrational spectrum directly linked to sample composition. This vibrational spectrum reveals characteristic information about the chemical bonds and structural environment of the molecules of interest. [44, 45] Additionally, the combination of Raman spectroscopy with optical microscopes yields spatial resolutions ranging from nm in near-field conditions to µm in far-field measurements, which enables mapping the distribution of molecules across a specific sample, such as a biological tissue or cell. Despite a weak signal due to a small scattering cross section, Raman scattering can be further enhanced by several orders of magnitude through surface effects, enabling shorter acquisition times under modest laser irradiances. Raman spectroscopy and its derivatives play an increasingly important role in biochemical and biomedical research, owing in part to its low sensitivity to water and its ability to provide detailed, label-free molecular information. Its capacity to resolve the structure and complexity of biomolecules—and to characterize the chemical composition of cells, tissues, and organs—is essential for advancing diagnostic technologies, developing effective therapeutic strategies, and informing disease prevention efforts. [46] Recent years have seen a rapid expansion in the use of Raman spectroscopy in therapeutic diagnostics, where it has been applied to the discovery of cancer biomarkers and the rapid, reliable screening of disease states.[47-50] Raman methods are routinely used to investigate biochemical changes associated with cancer, including alterations within the tumor microenvironment (TME).[51] For example, Kim et al.[52] developed gold-coated hexagonal-close-packed (HCP) polystyrene (PS) nanospheres for the diagnosis of breast cancer using human tears, which are a promising source of biomolecules.

View Article Online
DOI: 10.1039/D6AN00476H

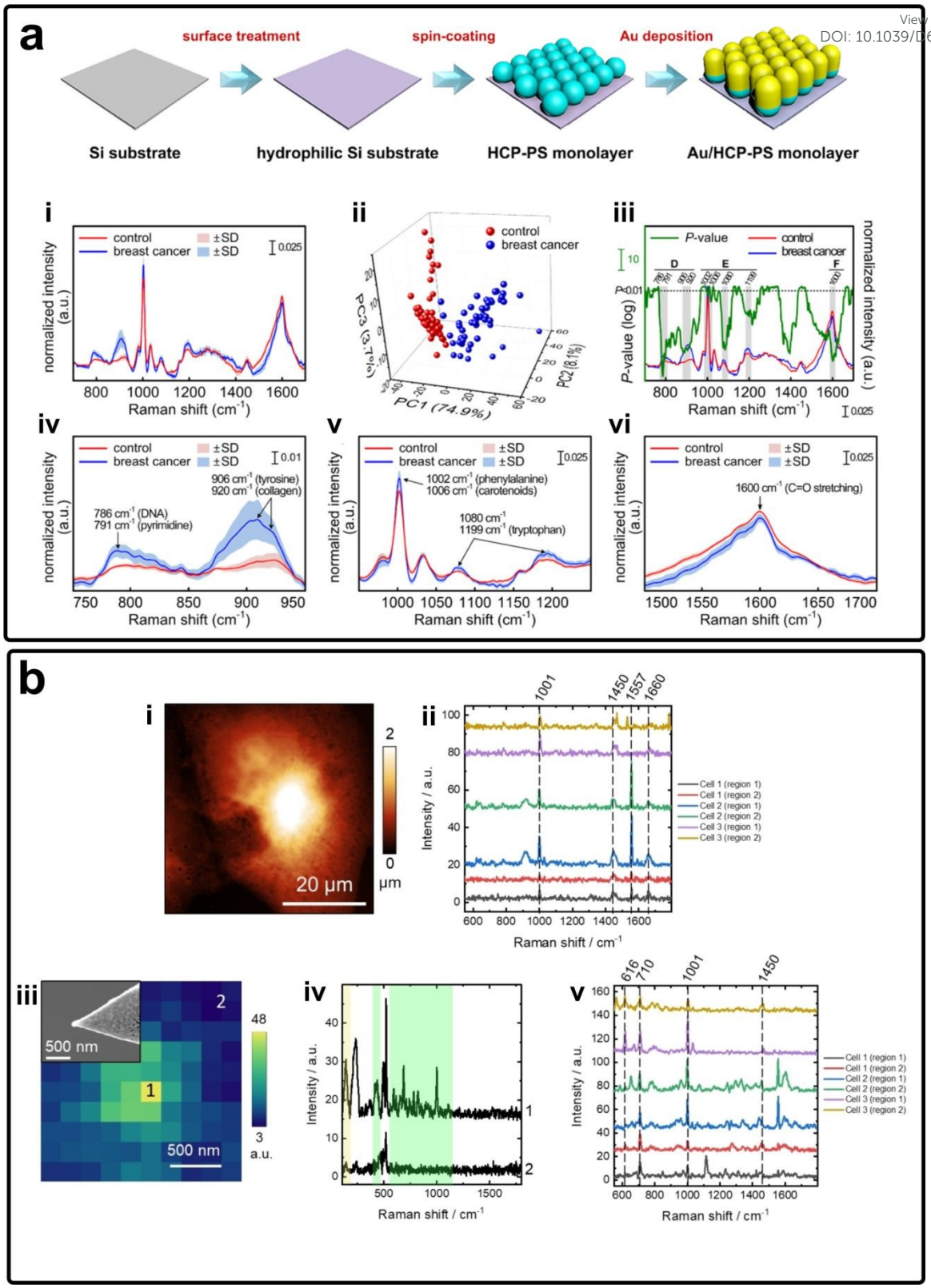

Figure 2. a) Fabrication of Au/HCP-PS Monolayer SERS Substrate, the corresponding SERS spectra and PCA analysis for control and breast cancer samples (i-ii), and the comparison for both populations in three different regions of the SERS spectra are presented (iii-vi). Adapted from reference [52] with permission of ACS Applied Materials & Interfaces (Copyright 2020, American Chemical Society). b) AFM topography for pancreatic cancer cells (i), Raman average spectra (n= 100) for the cells in two regions (ii), TERS hotspot (iii), Raman average spectra (n=10) in two regions (iv), and TERS spectra for three cells in different regions (v). Adapted from reference [53] licensed under CC BY-NC 4.0.

.

View Article Online
DOI: 10.1039/D6AN00476H

Their Au/HCP-PS monolayer platform generated strong, reproducible Raman enhancement and demonstrated the ability of SERS to quantify relevant biomarkers (**Figure 2a**). Conversely, Mrđenović, et al.[53] used tip-enhanced Raman spectroscopy (TERS) on human cell membranes derived from pancreatic cancer cells (BxPC-3), employing a plasmonic AFM probe to achieve nanometric spatial resolution and map the nanoscale distribution of intracellular biomolecules. Their TERS measurements revealed localized variations in phenylalanine, histidine, phosphatidylcholine, protein, and cholesterol domains, providing a chemically detailed view of subcellular organization (**Figure 2b**). Together, these studies demonstrated how advanced Raman techniques can analyze biomolecular composition from individual protein markers to nanoscale cellular structures, laying a solid foundation for their increasing use in the molecular characterization of extracellular vesicles (EVs) and their biologically active cargo.

This review focuses on recent advances in the study of cancer-derived EVs using: (i) conventional Raman spectroscopy, (ii) surface-enhanced Raman spectroscopy (SERS), and (iii) tip-enhanced Raman spectroscopy (TERS). We first provide a brief introduction to each technique and discuss recent studies leveraging vibrational spectroscopy and nanostructured substrates to enhance Raman sensitivity. We then emphasize how the integration of machine learning has become a powerful approach for analyzing complex Raman datasets, improving the accuracy, reproducibility, and diagnostic performance of EV-based sensing. Finally, we outline emerging trends and future directions in nanoscale infrared characterization of extracellular vesicles.

2.1 Raman-Based Vibrational Spectroscopy Techniques for EV Detection Using Plasmonic Platforms

Understanding cancer-derived extracellular vesicles (EVs) demands analytical tools capable of probing nanoscale biochemical heterogeneity with high sensitivity. Raman spectroscopy offers intrinsic molecular fingerprints, while its advanced modalities, when combined with engineered nanoplatforms, enhance sensitivity, spatial resolution, and diagnostic performance.

2.1.1 Conventional Raman Spectroscopy

Modern Raman spectrometers are most commonly used in conjunction with an optical microscope equipped with a confocal detection scheme and CCD or EMCCD detectors. Their spectral resolution depends on the grating used and the focal length of the apparatus, while the spatial resolution depends on the wavelength used and the numerical aperture of the objective (**Equation [1]**). The Rayleigh criterion is generally used as an approximation of the spatial resolution.

$$\Delta x = (0.61\ \lambda)/NA \quad [1]$$

Where Δx is the capacity to separate optically two objects located at Δx from each other, λ is the wavelength of excitation, and NA is the numerical aperture of the objective, ranging typically for a 100x objective from ~0.9 for dry objectives to over ~1.4 for immersion objectives. The theoretical spatial resolution yields values that range typically from ~230 nm (at λ=532 with NA=1.4) to ~530 nm (at λ=785 with NA 0.9), depending on the wavelength and objective used, which is compatible with the dimensions of individual apoptotic bodies and ectosomes.

The collected signal from the EVs corresponds to its membrane, primarily showing protein and lipid signals as well as its cargo that contains genetic materials, metabolites, and enzymes, as described previously in **Figure 1a**. Regarding the lipids that form the membrane, the polar part of the phospholipids has a characteristic peak at 720 cm^{-1} due to the vibration of the C-N bonds, while the hydrophobic tails have C-C skeletal vibrations around 1000 and 1150 cm^{-1}. In addition, the C-H stretching of the methylene chain groups shows two additional Raman contributions at 2880 cm^{-1} (asymmetric C-H stretch) and at 2850 cm^{-1} (symmetric stretching). Other significant bands include unique vibrational signatures of proteins, which allow the identification of specific amino acids and structural features. As an example, tyrosine shows Raman bands around 830 and 850 cm^{-1}, while peaks for tryptophan can be observed at 1014, 1338, 1361, and 1553 cm^{-1}. On the other hand, Raman modes coming from phenylalanine can be observed at 1006 cm^{-1}. In addition, recent studies have linked collagen to the spreading of tumor across various cancer types. Although present in smaller amounts, elastin can interact with collagen and other fibrous components to help form a dense extracellular matrix, facilitating cancer progression and invasion.[54] Typical Raman spectra of elastin and collagen show strong amide III vibrations in the 1250 - 1270 cm^{-1} range and a prominent amide I mode near 1650–1660 cm^{-1}. Regarding nucleic acid cargo, characteristic vibrational Raman bands are associated with the pyrimidine and purine bases. Typically, the pyrimidine bases (cytosine and thymine) exhibit a strong breathing mode around 770 cm^{-1} and a clear band at 1240 cm^{-1}. In contrast, for the purine bases (adenine and guanine), a strong breathing mode near 670 cm^{-1}, along with some peaks at 1480 and 1570 cm^{-1}, is observed. These Raman modes belong to the 1100–1700 cm^{-1} region, which is rich in Raman-active bands due to nitrogen base vibrations.[55] Additionally, the O–P–O symmetric stretching vibration appears close to 800 cm^{-1}, although its exact position can vary depending on the nucleic acid conformation. Finally, sugar components also contribute with some weaker signals around 800 and 1100 cm^{-1} and exhibit a CH_2 deformation band from the pentose ring at 1460 cm^{-1}.[56, 57]

Several studies have been conducted using conventional Raman spectroscopy to discriminate between the Raman fingerprints of healthy and malignant-derived EVs. Interestingly, it is possible to observe specific Raman peaks that can be used for

View Article Online
DOI: 10.1039/D6AN00476J

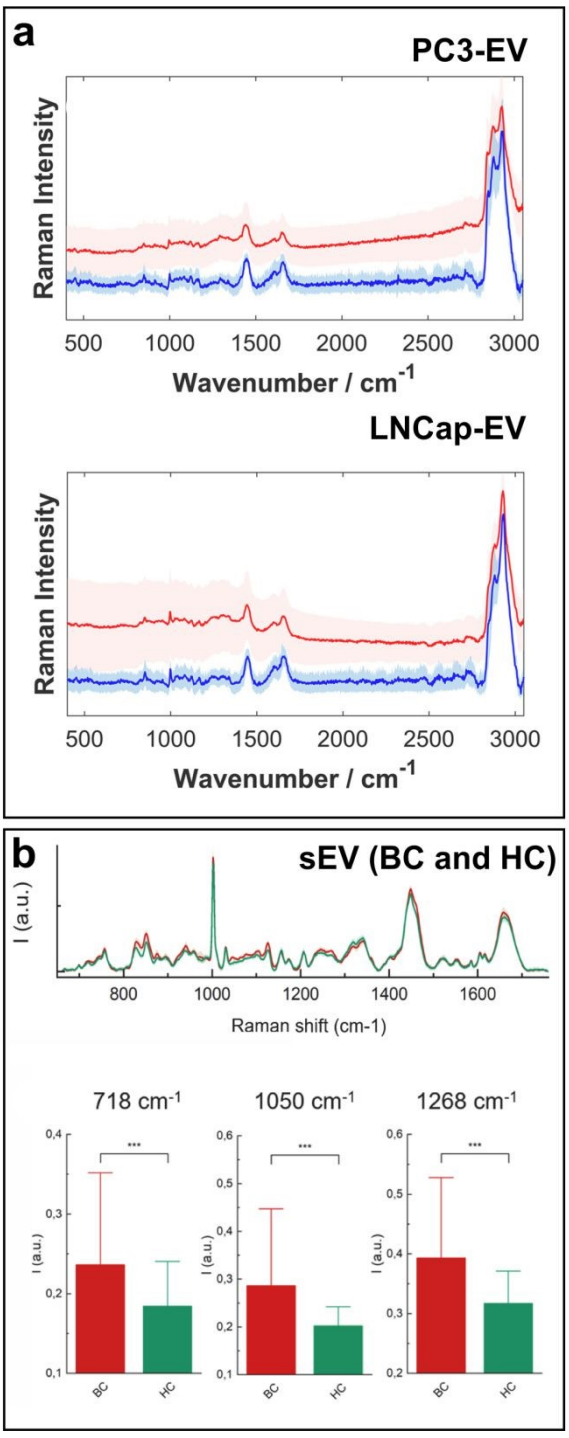

Figure 3. Average Raman (red) and collective Raman (blue) spectra of PC3 and LNCap. Adapted from reference [58] licensed under CC BY-NC 4.0. b) Average Raman spectra collected from BC (red) and HC (green) samples, as well as the statistics bar plots for selected peaks in both samples. Adapted from reference [59] with permission of Biosensors and Bioelectronics (Copyright 2025, Elsevier).

diagnostic purposes. For instance, Lee et al. [58] compared the Raman spectra of EVs derived from red blood cells, platelets, prostate cancer cell line 3 (PC3), and lymph node carcinoma of the prostate (LNCap). Here, about 300 Raman spectra were collected, and characteristic peaks were observed in the region of 1000-1700 cm-1 (**Figure 3a**). The analysis of Raman spectra was conducted by the use of a convolutional neural network algorithm (CNN), demonstrating an accuracy of 93%. More recently, Bonizzi et al.[59] obtained the Raman fingerprints of different variations of EV, including large and small EVs (lEVs and sEVs, respectively), high- and low-density lipoproteins (HDL and LDL). LPs showed typical Raman modes of lipids, such as cholesterol (698 cm^{-1}), and phosphatidylcholine (718 cm^{-1}). In contrast, EVs exhibited more intense peaks related to DNA and RNA around 746 cm^{-1} and 828 cm^{-1}. While Raman peaks of amino acids, such as tryptophan, were observed at 758 cm^{-1}, 1344 cm^{-1}, and 1552 cm^{-1}. In addition, phenylalanine modes were also obtained at 1003 cm^{-1} and 1030 cm^{-1}. Later on, the authors also compared real samples isolated from patients with breast cancer (BC) and healthy controls (HC). Here, 3 main Raman bands were recognized as the ones that differentiate between the healthy and cancer samples (718, 1050, and 1268 cm^{-1}) (**Figure 3b**).

2.1.2 Surface-Enhanced Raman Spectroscopy (SERS)

Surface-enhanced Raman spectroscopy was first discovered by Fleischmann et al. in 1974[60], who observed Raman signals coming from pyridine deposited at the surface of a silver electrode. In this work, the large enhancement in the signal was attributed primarily to an increase in the surface area from the roughness. However, years later, studies from Van Duyne et al.[61] and Albrecht et al.[62] demonstrated that this enhancement, which ranged from about 10^5 to 10^6, can not be explained by the sole effect of surface area increase. Subsequently, Moskovits explained the relationship between SERS intensities and the localized enhancement of the electromagnetic (EM) field originating in metal nanostructures and referred to as a localized surface plasmon (LSPR) mode.[63, 64] Since the initial SERS discovery, fundamental and applied work harvesting the SERS effect has constituted a whole research branch. SERS provides an alternative to counteract the weakness of the detected Raman signals due to the particularly small Raman scattering cross-section (~10^{-30} photons/cm^2/sr). As a result, Raman experiments generally require long acquisition times to yield a good signal/noise ratio. In addition, interference due to fluorescent background can be detrimental to the detection of Raman signals, especially when biological samples are analyzed. For isolated conductive nanomaterials, the LSPR is observed when an incident light of a given wavelength interacts with the free electrons of a metallic nanostructure, inducing their oscillation.[65] In the vicinity of nanostructures, the EM enhancement is confined in the surroundings of the nanostructure, creating small regions that are referred to as "hot spots". [66, 67] The activity of these hotspots and the spatial localization of the EM enhancement depend on the opto-geometric factors of the SERS platform (size, shape, density, index of refraction) and the irradiation parameters (frequency, polarization). LSPR can be tuned finely using advanced fabrication methods.[68, 69 70] The SERS effect is observed when a Raman active molecule is localized within these regions; the resulting Raman modes are amplified by a $10^6 - 10^8$ fold factor, even in the presence of a complex matrix.[69] The enhancement factor (EF) is the result of a predominant electromagnetic

View Article Online
DOI: 10.1039/D6AN00476H

enhancement (EM) together with chemical enhancement associated with the electron transfer between the molecule and the metallic SERS platform.

2.1.2.1 Bottom-up Synthesis for SERS Substrates

Over the years, researchers have increased the use of colloidal nanoparticles as SERS substrates for biomedical applications, including cancer diagnosis and biomarker detection. [71, 72] For instance, Xie et al.[73] designed SERS nanotags to characterize pancreatic cancer-derived EVs. In this work, three specific EV receptors were detected, and cell lines of pancreatic, colorectal, and bladder cancer were analyzed, exposing different phenotypes, allowing their differentiation. Breast cancer EVs isolated from serum biofluids were also analyzed by SERS using gold nanostars as the nanosurface. Here, SERS spectra of 4 cell lines for breast cancer were collected and inspected, enabling the diagnosis of this cancer and information about the post-operative results in the patients (**Figure 4a**).Lately, the use of SERS as a powerful technique for EV characterization was exploited by Shin et al.[74] by developing a multiplex platform based on gold nanoparticles to distinguish 6 different cancer types (lung, breast, colon, liver, pancreas, and stomach). The data was analyzed with an advanced neural network (NN) algorithm. The advantages of this innovative SERS chip rely on the detection time (1 hour) and highlight the use of EVs as potential diagnosis tools that not only discriminate between cancer types, but also early stages of cancer (**Figure 4b**). Although several studies focus attention on the use of colloidal nanoparticles for SERS measurements, these materials also show some disadvantages. An important drawback of nanoparticles is their tendency to aggregate, especially under different pH, salt concentration, or temperature, which affects their stability. In addition, the synthesis of different batches and the lack of uniformity can compromise the reproducibility of the experiments. Thus, spectral fluctuations can be detrimental for SERS diagnosis, principally when complex and heterogeneous matrices, such as EVs, are analyzed. To enhance selectivity, the nanoparticle surface can be further functionalized with molecules that can identify specific proteins or biocomponents in the extracellular matrix.[75-79] In this regard, the functionalization of the SERS substrate is achieved by the addition of antibodies that not only recognize but also capture inside the arrays the tumoral-derived EVs. As an example, AuNPs were functionalized with a Raman probe and then conjugated with anti-EpCAM and anti-CD125 antibodies for EVs derived from ovarian cancer.[78] In the same way, instead of antibodies, the use of thiolated aptamers has been spreading around the community due to their well-known high stability. Aptamers for HER2 and EpCAM were tested with AuNPs@Ag nanoparticles for the identification of breast cancer exosomes.[80]

2.1.2.2 Top-Down Fabrication of SERS Platforms

Reproducibility of SERS platforms that display the same performance is still an issue, in particular when using colloidal

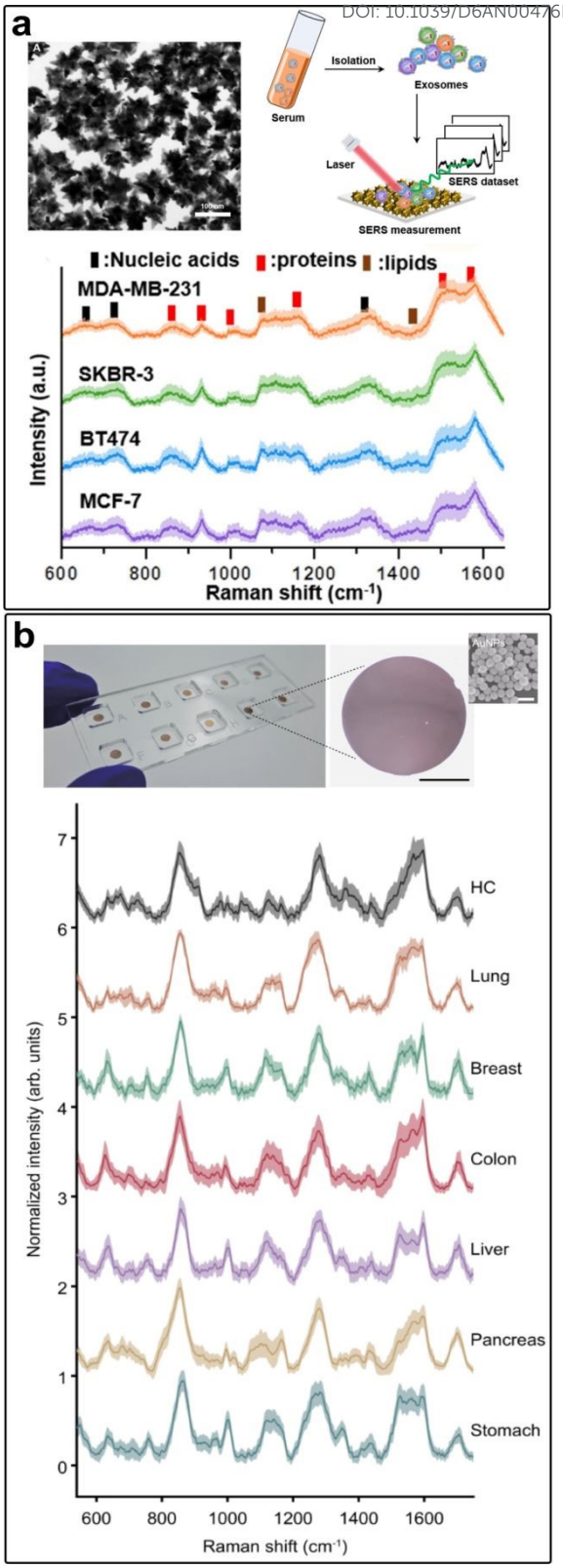

Figure 4. a) TEM of the gold nanostars synthesized to characterize the 4 cell lines of breast cancer. Adapted from reference [73] with permission of Nano Letters (Copyright 2022, American Chemical Society). b) Average Raman spectra collected from 6 different cancer types derived EVs using SERS chip based on gold nanoparticles. Adapted from reference [74] licensed under CC BY-NC 4.0.

View Article Online
DOI: 10.1039/D6AN00476H

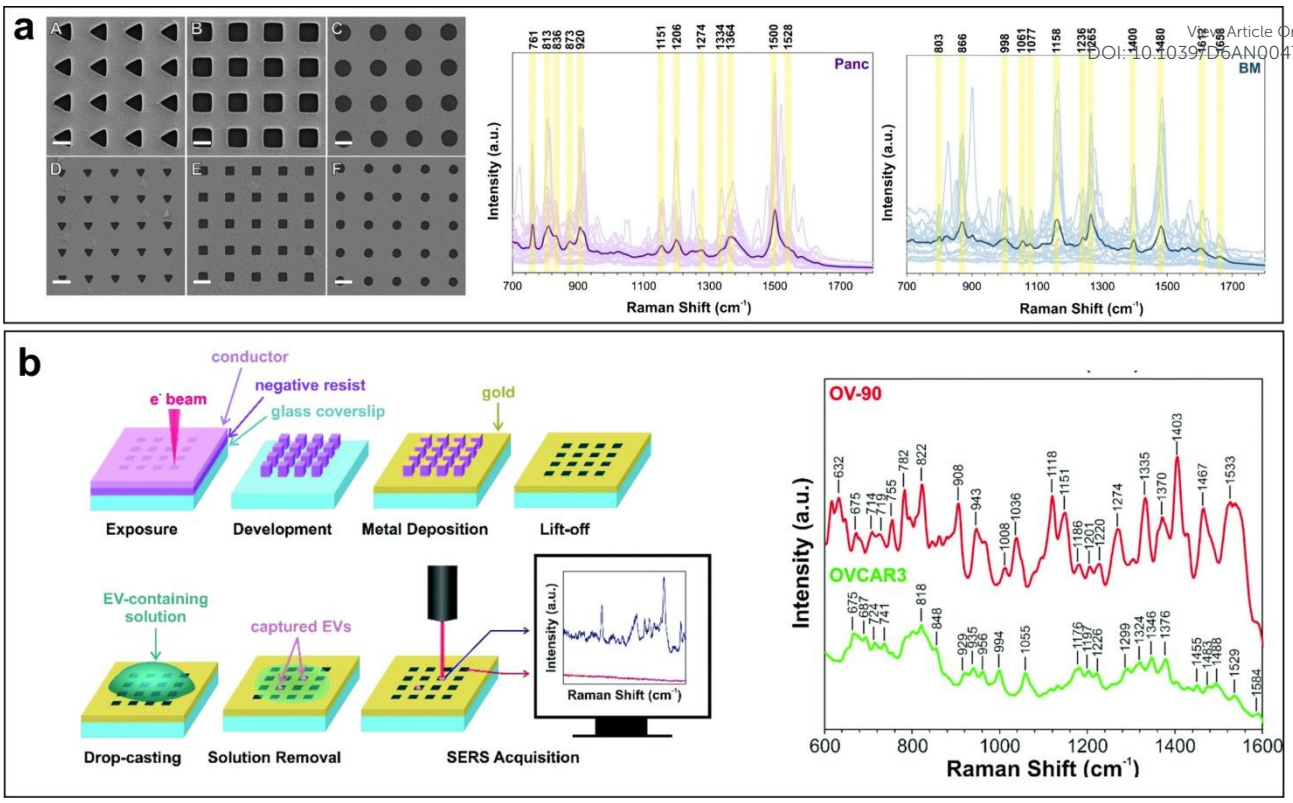

Figure 5. Nanohole arrays with different shapes and sizes were fabricated to characterize EVs isolated from pancreatic and bone marrow tissue. Adapted from reference [88] with permission of Analytical and Bioanalytical Chemistry (Copyright 2021, Springer Nature). b) EBL process to the development of nanohole arrays as a novel platform for ovarian cancer EVs derived from different cell lines. Adapted from reference [89] with permission of Analyst (conveyed through Copyright Clearance Center, Inc.).

particles. In this context, the use of advanced nanofabrication methods to create highly reproducible structures is of interest. [76, 77, 81, 82] Electron beam lithography (EBL) has the primary advantage of writing complex metallic patterns with a resolution of 10 nm, yielding a regular distribution of hot spots with similar magnitude.[83, 84, 85] These characteristics yield uniform and reproducible Raman spectra from the EBL-made platform. This enables quantitative analysis with better suitability for diagnosis applications. Other nano and microfabrication techniques, such as Focused ion beam (FIB) and nanoimprint lithography, can be used for the production of regular patterns that can be optimized for specific wavelengths and samples of interest. [86] An example of nanofabrication is the nanopillars designed by Jalali et al.[87] to detect exosomes derived from glioblastoma. Here, nanohole arrays were fabricated by EBL onto a MoS_2 surface. The novel design was embedded in a microfluidic device to obtain a single EV signal by SERS, achieving 97% confinement of the EVs on the array. The use of EBL and FIB was also employed for the creation of nanohole arrays (NHA) that can serve for both SERS and trapping of the EVs. Ćulum et al.[88] showed the design of a novel SERS platform with nanohole cavities for characterizing EVs isolated from mesenchymal stromal cells derived from pancreatic (PAN-EV) and bone marrow tissue (BM-EV) (**Figure 5a)**. These NHA platforms highlighted efficient trapping of EVs with minimal sample preparation, together with homogeneous and reproducible SERS enhancement, and high specificity. These NHA platforms were implemented for the characterization of EVs derived from ovarian cancer cell lines (**Figure 5b**). EVs isolated from OVCAR3, OV-90, high-grade (EOC6), low-grade (EOC18) serous cell lines, and human immortalized ovarian surface (hIOSE) as a control were deposited on the nanohole arrays and analyzed by SERS. [89] As a result, these platforms show interesting potential for diagnosis and for obtaining a single EV profile using a simple, label-free protocol. Furthermore, there is a growing trend to integrate simple nanohole substrates into microfluidic devices to develop portable Lab-on-a-Chip systems for real-time measurements. In summary, both bottom-up and top-down fabrication of SERS substrates are complementary routes for the investigation of EVS under Raman confocal microscopes.

2.1.3 Tip-Enhanced Raman Spectroscopy (TERS)

Despite the advantages offered by SERS in terms of signal enhancement, the spatial resolution of the Raman measurements in the vicinity of the EVs is limited to single EVs. [90, 91] To surpass the spatial resolution of Raman spectroscopy coupled to a confocal microscope, tip-enhanced Raman spectroscopy provides a breakthrough where the spatial resolution is only limited by the dimension of the metalized AFM tip that scans the object of interest. This concept, proposed by Wessel et al.[92] around 1985, is based on the use of a single nanoparticle that acts as an antenna concentrating the excitation light. In TERS, the extremity of the AFM probe acts as the particle that scans the surface. Following the attempts of

View Article Online
DOI: 10.1039/D6AN00476H

Wessel to improve spatial resolution, many research groups tested different combinations of Raman setups with AFM and STM. It was around the 2000s that the TERS field took off with the pioneering work of Stöckle et al., Hayazawa et al., Anderson et al., and Pettinger et al. [93-96] The principal strength of TERS is its capacity to obtain topographical information similar to what would be provided by an ordinary AFM or STM, along with spectral information and nanometric spatial resolution. In TERS, plasmonic oscillations are produced when a metallic tip (coated with Au or Ag)[97] is illuminated with a focused laser beam with the proper polarization.[90] The LSPR mode confined at the extremity of the tip is then scanned over the sample, yielding a collection of spectra and a subsequent sample map with resolution in the vicinity of 10 nm in ambient conditions. [44, 90] To obtain the near-field Raman signal in a TERS experiment, measurements are typically performed in two steps. As previously described, when the excitation beam illuminates the AFM cantilever while the tip is in close proximity to the sample, localized surface plasmon resonances are excited at the tip apex. This generates an enhanced near-field Raman signal. At the same time, however, the laser also produces a conventional far-field Raman contribution from the entire focal spot. Thus, in this first step (tip-in), the detected spectrum contains both near-field and far-field components. In the second step (tip-out), the cantilever is retracted so that it no longer provides enhancement. Although the sample is still illuminated, only the far-field Raman signal is recorded, with no contribution from the near-field. The near-field Raman contribution is generally obtained by subtracting the tip-out spectrum from the tip-in spectrum, although the tip-in measurements can show a much larger signal than the tip-out measurements. [90, 91, 93]

The selection of the proper substrate plays a crucial role in TERS experiments. To achieve a high enhancement of the signal, good spatial resolution, and reproducibility, the TERS substrate should be designed to produce a strong electromagnetic interaction with the AFM probe. Thus, thin flat films and platelets made of gold or silver are commonly used as substrates to provide further enhancement through gap-mode TERS measurements.[97-99] There are only a limited number of published works on EV characterization using TERS despite its well-adapted spatial resolution for EVs and cell sensing. A recent study by Zenobi's group[100] shows chemical imaging of cell membranes extracted from human pancreatic cancer using TERS. Domains identified in this approach contained phenylalanine, cholesterol, and other proteins in the EV surface. Similarly, Buccini et al.[101] use TERS to characterize milk-derived EVs and, one more time, differentiate lipids and proteins at the surface of EVs, completing previous work. The use of bovine milk mimics the complexity of a dense biofluid but also contains other protein aggregates and contaminants that can affect the Raman spectra. Stepanenko et al.[102] successfully elucidated the chemical composition of lipid bilayers using a high-resolution map. The authors isolated extracellular vesicles from red blood cells and compared the fingerprints using SERS and TERS measurements. In this work, a flat gold film was used as a substrate, which, coupled with a gold AFM tip, produces gap-

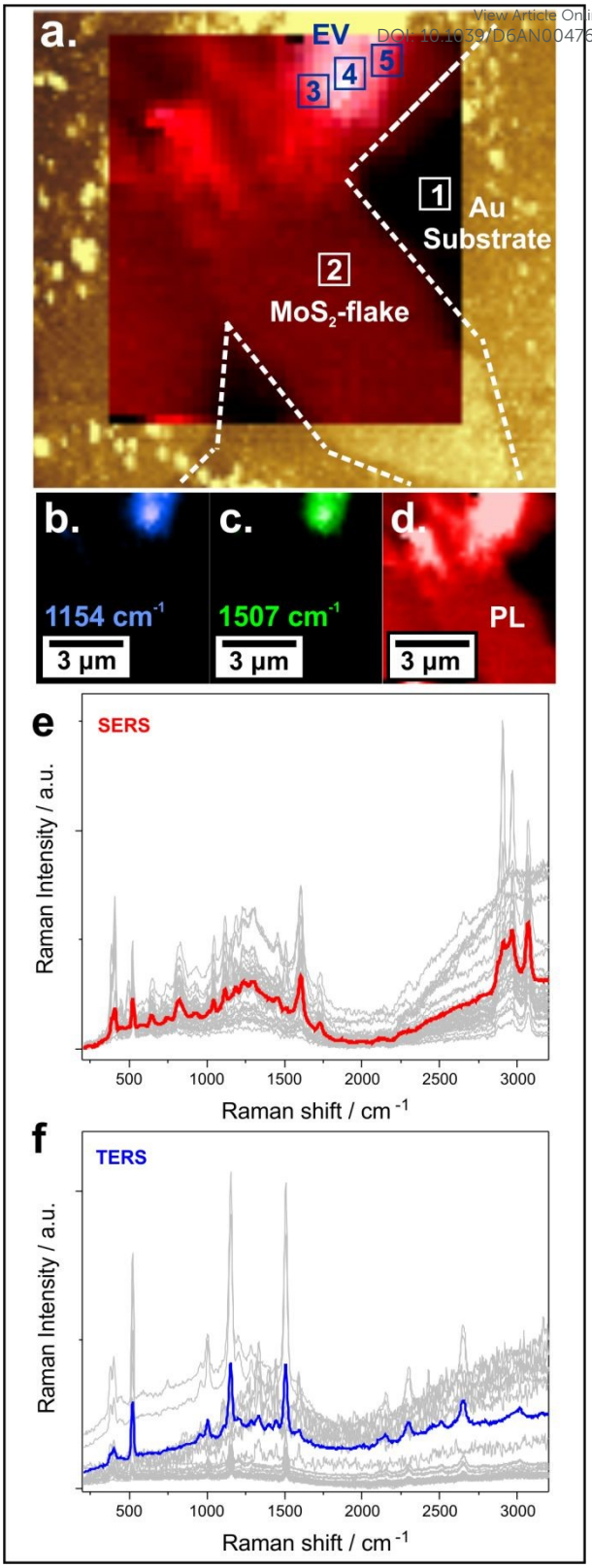

Figure 6. (a) AFM and overlay TERS maps showing the EVs on the surface of MoS_2. TERS maps showing the Raman modes coming from the strong EV signals at (b) 1154 cm^{-1} (blue) and (c) 1507 cm^{-1} (green), and (d) PL (red) originating from the MoS_2 flake. Comparative and average e) SERS and f) TERS spectra obtained (n=30). Adapted from reference [103] with permission of Nanoscale licensed under CC BY-NC 3.0.

View Article Online
DOI: 10.1039/D6AN00476H

mode TERS to maximize enhancement. Indeed, TERS characterization permits the nanoscale observation of protein and lipid domains on the EV membrane as well as heterogeneities in the EV cargo. Recently, the first approach for cancer-derived EVs was developed by Veliz et al.[103] Here, the authors demonstrated that TERS reveals hidden Raman modes and biochemical features of EVs isolated from plasma samples extracted from patients with high-grade serous carcinoma (HGSC) that can not be resolved by SERS measurements. Specific signals from proteins, lipids, and nucleic acids were obtained by using an Au-AFM probe and MoS_2 flakes deposited onto a gold substrate. With the TERS map overlayed with AFM image and the Raman modes at 1154 cm^{-1}, 1507 cm^{-1}, and PL, the authors resolved the location of a single-EV particle on the surface of a MoS_2 flake (**Figure 6a-d**). These measurements also highlight distinct vibrational signatures from SERS and TERS (**Figure 6e-f**) due to the different selection rules and setup polarizations. TERS appears to be well adapted to the study of isolated biological objects such as EVs.

3. Integration of Machine Learning for Data Processing

Despite the several advantages of SERS and TERS, interpreting their spectra remains complex because the datasets consist of thousands of Raman spectra, each with thousands of points. In this regard, computational tools, including machine learning methods, have been widely used in recent years. In this context, machine learning is an advanced technique rooted in artificial intelligence that involves creating various algorithms to classify data efficiently and reliably. The primary aim of machine learning is to utilize hidden patterns within a dataset to discover statistical regularities, enabling the classification, prediction, and establishment of correlations that mimic human brain functions. Different approaches have been devised to analyze and classify diverse types of spectroscopic data, with the most significant being unsupervised and supervised learning algorithms. We briefly review these approaches in the context of EV classification

3.1 Unsupervised Algorithms for Classification

Unsupervised algorithms such as PCA focus on forming clusters from uncategorized data. In simple terms, the algorithm learns to identify feature correlations in the collected dataset to group them by similarity. PCA transforms the full spectral data set into a simple and smaller group of orthogonal variables that are known as the principal components that will retain the maximum variance while keeping critical spectral information. PCA is commonly used, revealing important details and patterns from large data sets for classification in spectral groups.[104, 105]
Another advantage of PCA is the capacity to reduce the dimensionality of the data even in the absence of labels. This means that the algorithm can cluster data just by distinguishing minimal differences in the Raman spectra. One example was the work presented by Koster et al.[106] based on the analysis of EVs derived from head and neck carcinoma and their possible contamination with lipoproteins. Three isolation methods were tested: ultracentrifugation (UC), density gradient ultracentrifugation, and size-exclusion chromatography (SEC). Each sample was analyzed by SERS, and the collected data were classified using PCA. Important findings demonstrated that major contamination due to lipoproteins depends strongly on the isolation methods, and double isolation procedures may ensure a pure EV fraction. In a different approach by the same group, amyloid β in EVs was identified by combining Raman spectroscopy and PCA analysis using principal components 1 and 2. The detailed analysis differentiated healthy controls from EVs enriched with amyloid β and identified signals supporting the model, such as the amide I (1650 cm^{-1}) and CH (2930 cm^{-1}) vibrations. The limitation here was the low intensity in the Raman modes, which can be solved by the addition of nanostructures, as was discussed in the previous sections. [107]

Several SERS studies were also conducted using magnetic nanoparticles. As an example, Li et al.[108] functionalized superparamagnetic nanoparticles with biotin-anti-CD9 antibody to recognize specific cell lines from breast cancer (MCF-7 and MDA-MB-231), 6 serum-EVs from healthy patients, and 14 from breast cancer patients. This study highlighted PCA results showing that PC1 and PC2 accounted for 96.9% and 2.4%, respectively. The magnetic SERS platforms achieved 100% specificity and 91.6% sensitivity in classifying healthy vs. cancer samples (**Figure 7a**).

Russo et al.[109] demonstrated that combining SERS with PCA enabled reliable discrimination between precursor states and two types of myeloma malignancies, highlighting the importance of linking spectroscopic sensitivity with multivariate statistical analysis. Blood samples from 31 patients were collected and processed to extract the corresponding EVs (**Figure 7b**). Overall, such research emphasizes the potential of spectroscopic profiling as a non-invasive method for disease classification. Building on these developments, recent efforts have shifted towards machine learning methods, which go beyond PCA to utilize complex spectral patterns and achieve improved diagnostic accuracy.

3.2 Machine Learning Algorithms

While PCA is an unsupervised algorithm focused primarily on reducing spectral data while preserving key patterns, machine learning (ML) is a set of algorithms and mathematical functions designed to learn from and gain experience with training datasets, automating decision-making, and predicting and classifying. In general, supervised methods use part of the data as a training subset to build functions that reduce the computational time needed to predict and classify a specific attribute. Once the process finishes, the algorithm compares the results obtained with the predicted results, identifying possible misclassifications or errors and adjusting the model until acceptable performance is achieved.[87-89, 110-112]
To build an ML model, there are three important steps to follow after collecting the desired Raman data. First, data

View Article Online
DOI: 10.1039/D5AN00475H

preprocessing is applied to clean the dataset of artifacts such as cosmic rays and electronic noise from the detector, and to smooth or remove the fluorescence background. Pre-processing steps can include normalization or standardization of data to ensure comparability and analysis of possible outliers. Due to the massive information contained in a Raman dataset, PCA can be first selected chosen as a pre-processing step to reduce the data, improving the efficiency of the ML model.

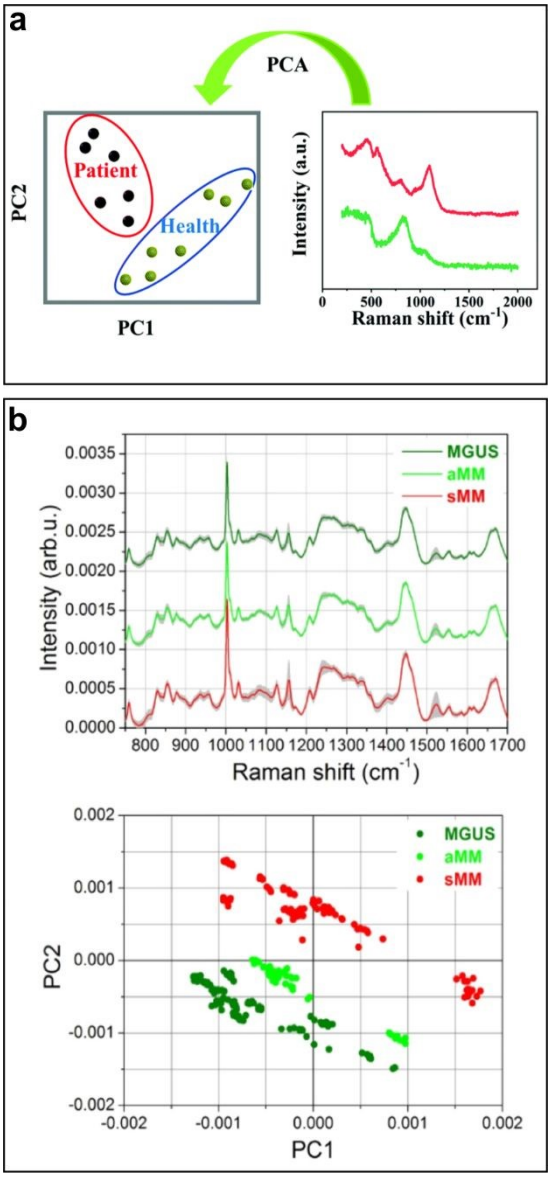

Figure 7. (a) PCA results showing the varying levels of PC1 and PC2 to be 96.9% and 2.4%, respectively, for breast cancer and healthy patient samples. Adapted from reference [108] with permission of Journal of Materials Chemistry B (conveyed through Copyright Clearance Center, Inc.). b) The performance of the magnetic SERS platforms in discriminating between precursor and two categories of myeloma malignancy. Adapted from reference [109] with permission of ACS Omega (Copyright 2020, American Chemical Society).

Once preprocessing is completed, the development of the ML model involves the separation of the data set into three groups: the training set, the validation and the test data set. To select the appropriate ML algorithm, it is important to analyze what is the principal goal of our model. For instance, algorithms like partial least squares regression (PLS) are suitable when there is a strong correlation between the independent and dependent variables, as in the case of predicting the concentration of bacteria or toxins in water or food crops.[113, 114] Another common algorithm that allows spectral classification is K-means clustering (KNN), which is governed by the principle that similar points tend to group. KNN is applicable for large data sets, is sensitive to the presence of outliers, and requires that the number of clusters be pre-defined before doing the modelling. This algorithm has been used for the identification of biomarkers and classification of cancer and healthy cells.[115]
Random Forest (RF) is another robust ML model which is based on decision trees to make predictions. RF is a robust algorithm and also suitable for large datasets like Raman spectra.[116] In contrast, a support vector machine (SVM) is focused on finding a hyperplane that best separates the data. In other words, it will find the best and optimal boundary between classes using a kernel function.[117] However, as in the case of RF, the optimization of the hyperparameters (e.g. number of trees, layers or kernel function) is key for the functionality of the algorithm.[118] On the other hand, Logistic Regression (LR) is a more straightforward ML model that gives easy-to-interpret results. LR works with kernel functions that transform the data in such a way that it is easier to analyze by the computer.[104, 110] By using a variety of these algorithms, del Real Mata et al.[110] developed a nanostructured platform to evaluate EVs derived from brain cancer (glioblastoma), achieving accuracy values of 83% and 91% in multi-cell line classification and healthy vs cancer differentiation, respectively. (**Figure 8a**)

Some ML models are considered deep learning algorithms, such as neural networks. As the name suggests, these kinds of algorithms try to mimic the behavior of the human brain. Artificial neural network (ANN) is one of the most recognized deep learning algorithms. It is based on the layers, which are connected by nodes or “neurons” that receive the information, assign importance based on the features, and give a conclusion. Thus, ANN is useful for managing complex data, but also requires a larger training dataset to be able to make the right prediction.[119] Following the same principle, a convolutional neural network (CNN) is a very suitable tool for imaging data. In CNN, the layer may extract important details regarding a particular image dataset, such as edges, textures, or shapes.[87, 112, 120]

Due to the spectral complexity of biological materials, machine learning models have become essential tools for extracting meaningful patterns from EV-derived data. As an example, surface and internal biomarkers of lung cancer cells were classified with 98.95% accuracy using a model based on two convolutional layers.[121] Here, the authors demonstrated how deep-learning architectures can resolve subtle spectral differences in the EV complex matrix that conventional analytical methods often overlook. EVs derived from the early stage of ovarian cancer were also tested by ANN, obtaining

View Article Online
DOI: 10.1039/D6AN00476H

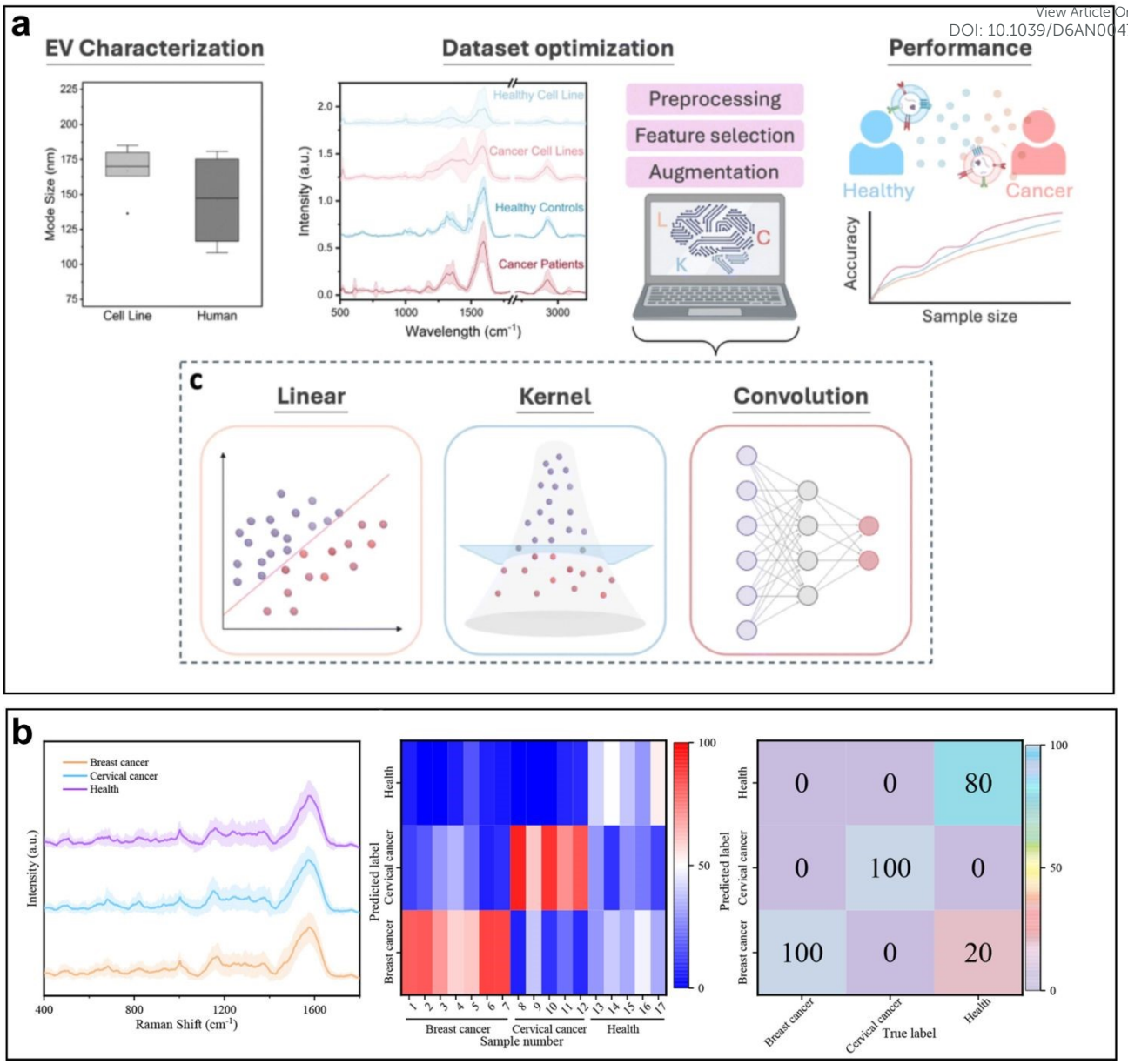

Figure 8. a) Flowchart for the analysis of EVs derived from glioblastoma, highlighting the characterization, data collection, and algorithm evaluation. Adapted from reference [110] licensed under CC BY-NC 3.0. b) SERS sensor developed for multiplex detection of breast cancer and cervical cancer. Adapted from reference [111] with permission of Analytical Chemistry (Copyright 2023, American Chemical Society).

promising results of 70.6% classification accuracy, 68.8% specificity, and 71.6% precision despite the heterogeneity and complexity of the real samples.[112] The results achieved in this work highlight the potential of machine learning to detect early disease signatures even when EV composition may vary widely across patients. Beyond single-marker analysis, multiplexed platforms combined with machine-learning classifiers have been developed to identify EV-associated cancer biomarkers, enabling simultaneous detection of more than three targets with high accuracy. These multiplex technologies were also fabricated to identify more than 3 specific cancer biomarkers[122] and different cancer types[111], including breast cancer and cervical cancer, with an accuracy of 93.3% (**Figure 8b**). As a result, these studies illustrate that coupling machine-learning algorithms with EV-based sensing platforms substantially improves diagnostic accuracy, enables earlier detection of malignant tumors, and helps address the analytical challenges associated with EV heterogeneity by discovering relevant patterns that correspond to EV subpopulations.

The combination of spectroscopy techniques such as Raman, SERS, and TERS with computational models is a powerful tool for spectral interpretation, revealing hidden details and managing large data sets. For these reasons, thanks to the high accuracy and precision in the final classification, these ML approaches are valuable for numerous applications, such as the diagnosis of cancer. Thus, the field of SERS-ML biosensors continues to develop with the creation of reliable, fast, and simple diagnostic systems.

View Article Online
DOI: 10.1039/D6AN00476H

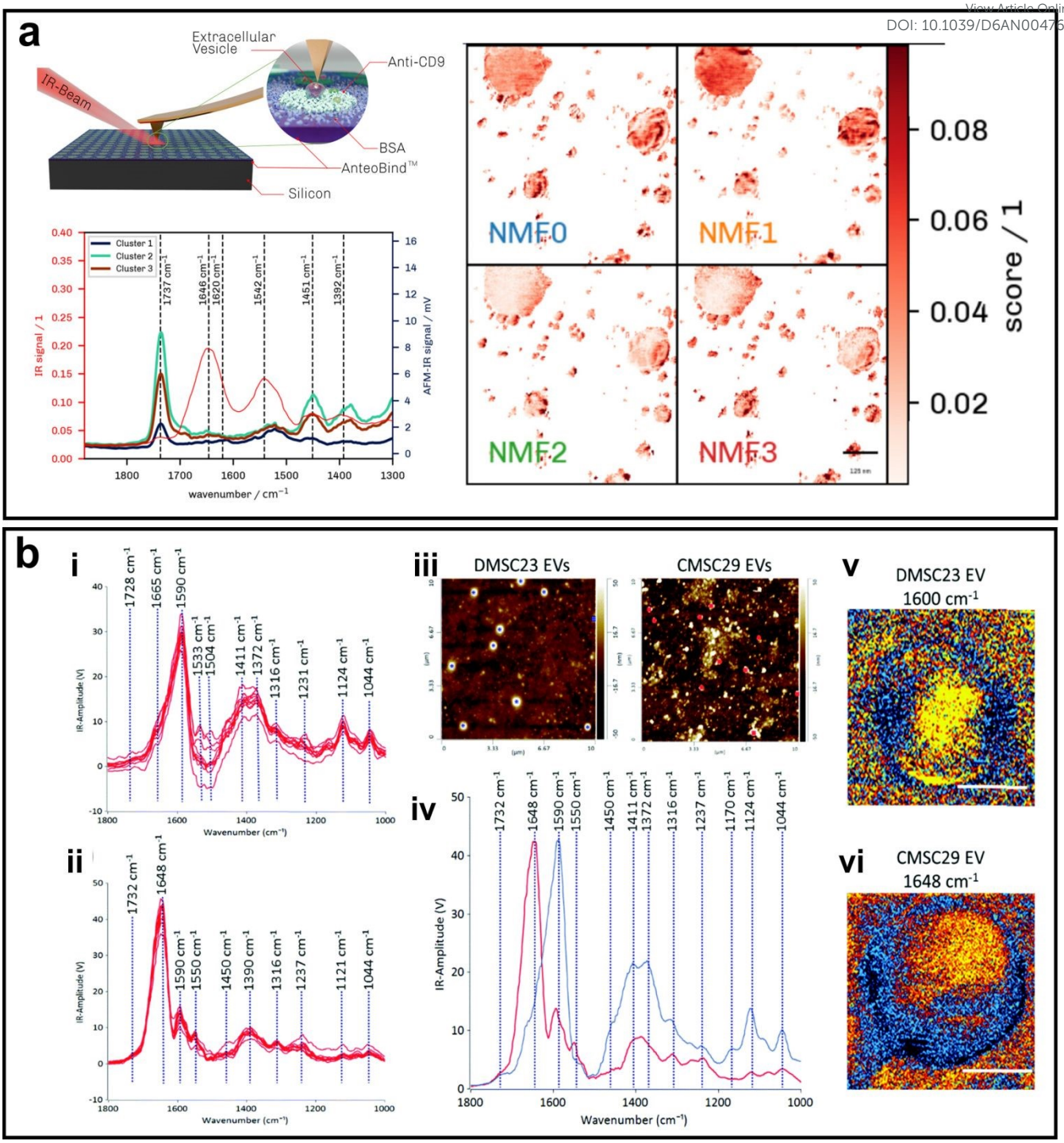

Figure 9. a) Representation of immobilized EVs on an antibody-functionalized silicon substrate. Also, spectra collected from multiple points within individual vesicles (cluster 1, 2, and 3) are compared with the reference bulk FTIR profile (red). Finally, the score plot visualizes the distribution of spectral clusters, illustrating distinct chemical signatures across captured EVs. Adapted from reference [128] licensed under CC BY-NC 4.0. b) Comparative IR spectra of DMSC23 (a) and CMSC29 (b), as well as the corresponding AFM images (c), average spectra and IR mappings (d-f). Adapted from reference [129] with permission of Nanoscale Horizons (conveyed through Copyright Clearance Center, Inc.).

4. Future perspectives

As the field of extracellular vesicle (EV) research continues to mature, there is a growing demand for analytical techniques capable of resolving EV heterogeneity with higher sensitivity, improved spatial resolution, and increased throughput. In parallel, recent advances in vibrational spectroscopy, together with machine-learning-assisted data analysis, have considerably expanded the methodological landscape available for EV characterization. In this review, we highlight selected emerging

View Article Online
DOI: 10.1039/D6AN00476J

spectroscopic approaches and discuss their potential as next-generation platforms for EV classification and phenotyping.

4.1 Resonance-Enhanced Atomic Force Microscope Infrared Spectroscopy (AFM-IR)

The introduction of AFM-IR (also referred as Nano-IR) marked an important milestone in the development of vibrational techniques with nanoscale resolution. In the early 2000s, the pioneering work of Dazzi et al.[123] demonstrated to the research community that an atomic force microscope (AFM) could be modified into a highly sensitive detector of infrared absorption with a spatial resolution significantly below the diffraction limit. The authors introduce a new spectroscopy modality by coupling a pulsed tunable IR laser to an AFM cantilever, enabling the acquisition of chemically specific information from nanoscale structures. This new design confirms AFM-IR's performance as a powerful analytical tool and paves the way for its rapid implementation across materials science and, especially, biological research.[123-125] Similar to TERS, the use of an AFM probe is one of the principal characteristics of AFM-IR. However, the principles are distinct. In TERS, the Raman scattering is enhanced by the electromagnetic field localized in the vicinity of the AFM tip apex. In contrast, AFM-IR measures the IR absorption, detecting the photothermal expansion of the sample through the AFM-probe oscillations.[123, 125] When the sample is illuminated with a tunable IR laser, regions that absorb at the specific wavelength produce a thermal response, which is transduced into resonant oscillations of the cantilever. Finally, the thermal response is converted to the corresponding IR spectrum by Fourier transformation. Moreover, the penetration of an AFM-IR tip is several hundreds of nanometers compared to TERS, leading to a deeper analysis of the sample.[126] As a result, AFM-IR enables the acquisition of point spectra and chemical maps with nanometre-scale spatial resolution together with the surface topographical information.

Recently, the applications of AFM-IR have spread to different fields such as life sciences, drug delivery, and biological analysis.[126, 127] For this reason, AFM-IR has emerged as a technique of choice for probing the molecular composition of nanoscale structures, including protein aggregates, lipid domains, viruses, and extracellular vesicles (EVs).[128, 129] For instance, the work of Rizevsky et al.[126] demonstrated that AFM-IR could be used to reveal the core and outer shell of insulin fibrils, benefiting from the deeper penetration of the IR light source. This ability is of particular interest for the EV field because it may be possible to resolve EV lipid domains, identify protein secondary-structure signatures, and identify nucleic acid subpopulations within single EVs. The work of Hondl et al.[128] has shown a robust workflow for the chemical analysis of milk-derived EVs. Here, the immobilization of EVs in the silicon substrate by the CD9 antibody, combined with the tapping mode AFM-IR, allowed the collection of hyperspectral imaging of several EVs, revealing the distribution of lipids and proteins. Moreover, the application of chemometric analysis, such as non-negative matrix factorization (NMF) enables label-free, sub–vesicle–level chemical mapping of single EVs and the clear differentiation of each biomolecule domain (**Figure 9a**). Another example of the high spatial resolution of AFM-IR has been evidenced by the work of Kim et al.[129] In this case, EVs derived from mesenchymal stromal cell lines (CMSC29 and DMSC23) were isolated by SEC and characterized by AFM-IR. One of the first characteristics is that, despite the Ev-source, each cell line provides a unique fingerprint with characteristic vibrational modes (**Figure 9bi-ii**). Here, distinct protein, lipid, and nucleic acid modes including amide I/II variations (1648 cm-1), lipid ester peaks, and vibrational modes corresponding to thymine and purine nitrogen bases. The height profile and the Raman average spectra of CMSC29 and DMSC23 (**Figure 9biii-iv**) allow the comparison between both cell lines and the identification of the highest vibrational modes (1590 and 1648 cm^{-1}). These specific signals were later used to build the IR corresponding map for each sample (**Figure 9bv-vi**), demonstrating the efficiency of AFM-IR to profile single-EVs. In summary, by revealing structural and molecular heterogeneity that was previously inaccessible, AFM-IR is capable of differentiating between EV subclasses, allowing the detection and validation of spectral biomarkers correlated with a particular carcinogenic tumor or its stage, supporting the development of high-resolution EV-based diagnostic platforms. As such, AFM-IR represents a promising avenue in bioanalytical chemistry, offering nanoscale chemical precision that aligns closely with the emerging needs of EV research and clinical translation.

4.2 Microfluidic Devices for EV Isolation and Characterization

The first experiments behind a microfluidic chip started when Terry et al.[130] designed a gas chromatography prototype in a silicon substrate using photolithography and etching. Since then, microfluidic technologies have evolved as powerful analytical platforms capable of manipulating fluids at the micrometer scale with outstanding precision. Indeed, the use of microfluidic chips depends on precise control of small sample volumes (10^{-6} to 10^{-8}).[131] Simultaneously, these lab-on-a-chip devices are typically portable, allowing for rapid screening and diagnosis because of the small microchannels. The improvement in advanced nanofabrication techniques has made the design and manufacturing of microfluidics increasingly accessible, promoting its integration with mass spectrometry (MS), electrochemistry, and Raman spectroscopy, allowing the accurate manipulation of chemical or biological reactions.[132-134] Furthermore, combining these innovative chips with SERS enables the creation of reproducible and highly sensitive platforms, providing non-destructive yet highly quantitative and qualitative single-molecule analysis. Additionally, the continuous flow of samples across the microfluidic platforms helps prevent thermal heating from laser excitation and diminishes fluctuations in the Raman signal.[131, 134]

Among the many applications of microfluidic devices, biosensing is probably the one that has experienced the most rapid growth.[133] The unique advantages of SERS for identifying biomolecules such as proteins, lipids, or nucleic acids, combined

View Article Online
DOI: 10.1039/D6AN00476H

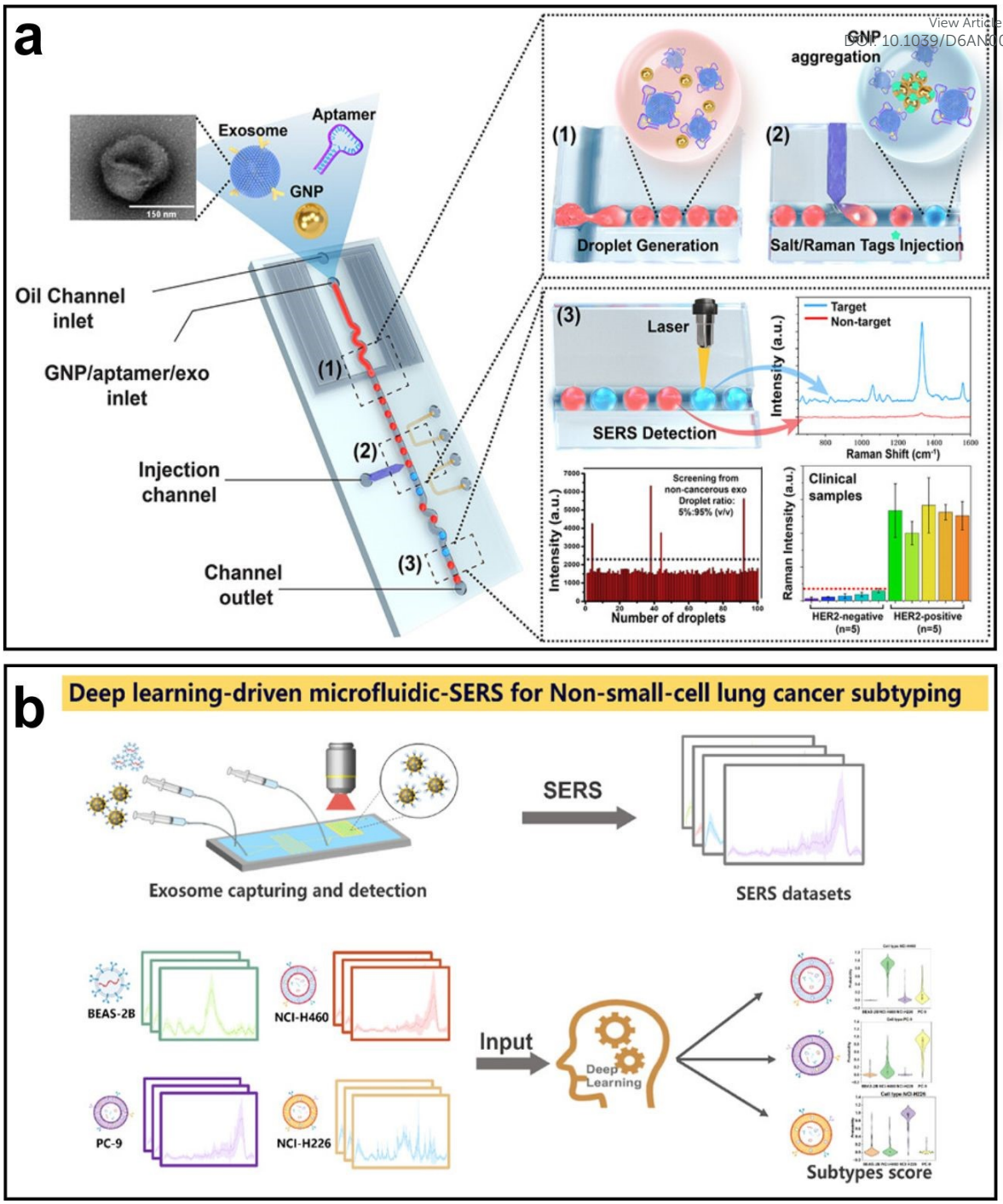

Figure 10. a) Representation of the SERS droplet-based microfluidic device for the targeting of breast cancer cells (HER2). Adapted from reference [75] with permission of ACS Sensors (Copyright 2024, American Chemical Society). b) SERS microfluidic platform for the detection of Lung cancer subtypes. Adapted from reference [136] with permission of ACS Sensors.

with the small yet well-controlled space in a microfluidic device, provide an ideal platform for biomedicine and in-situ biosensing applications, even with low sample volumes like those obtained from body fluids.[135] In EV research, microfluidic devices have emerged as an alternative to address key challenges associated with vesicle heterogeneity, low abundance, and the need for standardized isolation workflows. For instance, the work of Ho et al.[75] highlights a SERS droplet microfluidic platform for the detection of EVs derived from breast cancer(**Figure 10a**). In this case, the system is based on the recognition of SKBR3 exosomes through the functionalization of gold nanoparticles with HER2 aptamers. The introduction of salt induces nanoparticle aggregation, leading to the formation of a higher density of electromagnetic "hotspots" (**Figure 10a - zone 1-2**). These closely spaced junctions locally enhance the electric field, resulting in a substantial increase in the observed Raman signal at 1339 cm^{-1}. Interestingly, when compared with traditional approaches, this embedded SERS platform enabled the

View Article Online
DOI: 10.1039/D6AN00476H

identification of cancer exosomes at low concentrations (5% SKBR3) and yielded a lower limit of detection (LOD) of 3.2 x 10^4 particles/mL. Although short acquisition times per sample (5 min) were needed to complete the analysis with the droplet microfluidic device, it still showed great sensitivity to distinguish between positive SKBR3 exosomes and negative ones (**Figure 10a – zone 3**). Lastly, in 2025, Chen et al.[136] designed a microfluidic device with two chambers (mixing and trapping) to identify cell lines derived from lung cancer (**Figure 10b**). In this case, the capture of the EVs was achieved by gold nanocubes attached to polystyrene beads and functionalized with CD9-antibody. Normal epithelial cells derived from lung cancer (BEAS-2B) and human non-small cancer cell lines, including NCI-H460, NCI-H226, and PC-9, were monitored by SERS, collecting 944 spectra in total. This dataset was augmented to 2832 spectra by adding Gaussian white noise and was randomly divided into a training set and a test set in a 7:3 ratio. As a result, the final output of the device showed a promising efficiency of 85% calculated using deep learning algorithms and classifying 3 subtypes of non-small cell lung cancer with 97.9 % accuracy and an AUC of more than 0.95 for each one of them.

Both studies highlighted the advantages of microfluidic platforms lie in the enrichment of EVs based on size, density, or surface markers, obtaining higher purity yields than conventional ultracentrifugation or precipitation methods. At the same time, the combination of microfluidic SERS platforms and ML classification and spectral classification approaches increases the quality of the data set and improves the spectral analysis. As a result, microfluidic technologies represent a key avenue in analytical chemistry, offering scalable, reproducible, and clinically compatible solutions for EV isolation and characterization.

5. Conclusion

Extracellular vesicles (EVs) have emerged as central components of liquid biopsy, offering stable, information-rich fingerprints of disease state and progression accessible through minimally invasive sampling. This review has highlighted recent progress in vibrational spectroscopic approaches for EV analysis, with a particular focus on Raman-based techniques. Surface-enhanced Raman scattering (SERS) and tip-enhanced Raman spectroscopy (TERS) stand out as powerful methodologies, providing high sensitivity and nanoscale spatial resolution to probe both surface-associated biomolecules and intravesicle cargo in a label-free manner.

Although still at an early stage, the integration of machine learning with Raman spectroscopy represents a critical step toward extracting biologically meaningful information from large, complex spectral datasets. Continued advances in data-driven analysis are expected to improve spectral classification, enable more robust discrimination between EV subpopulations, and facilitate more accurate assignment of vibrational features to specific biochemical components.

Beyond Raman spectroscopy, emerging infrared-based techniques offer complementary capabilities for EV characterization. In particular, AFM-based infrared modalities exploiting photothermal or scattering mechanisms enable single-vesicle analysis with enhanced chemical specificity and depth sensitivity, opening new opportunities to interrogate EV heterogeneity at the nanoscale. These advances underscore a broader trend toward multimodal, high-resolution vibrational platforms tailored for single-particle analysis.

Finally, the incorporation of microfluidic technologies provides a critical pathway toward standardized, high-throughput EV handling. Microfluidic devices enable controlled sorting, trapping, and interrogation of individual EVs, facilitating consistent spectroscopic and correlative measurements across statistically relevant populations. The convergence of advanced vibrational spectroscopy, machine learning, and microfluidic integration is poised to transform EV analysis, bringing these methodologies closer to routine analytical and clinical implementation.

Author contributions

The manuscript was written through the contributions of all authors. All authors have approved the final version of the manuscript.

Conflicts of interest

There are no conflicts to declare.

Acknowledgements

This research (L.V. and F. L. L) was supported by the Natural Sciences and Engineering Research Council (NSERC) of Canada through a Discovery Grant (DG RGPIN-2025-05276).

References

1. C. M. Okeoma, *Viruses*, 2020, **12**, 1265.
2. E. Chargaff and R. West, *J. Biol. Chem*, 1946, **166**, 189-197.
3. Y. Couch, E. I. Buzàs, D. Di Vizio, Y. S. Gho, P. Harrison, A. F. Hill, J. Lötvall, G. Raposo, P. D. Stahl, C. Théry, et al., *J Extracell. Vesicles*, 2021, **10**, e12144.
4. G. Raposo, H. W. Nijman, W. Stoorvogel, R. Liejendekker, C. V. Harding, C. Melief and H. J. Geuze, *J. Exp. Med.*, 1996, **183**, 1161-1172.
5. Y. Couch, E. I. Buzàs, D. Di Vizio, Y. S. Gho, P. Harrison, A. F. Hill, J. Lötvall, G. Raposo, P. D. Stahl, C. Théry, et al., *J. Extracell. Vesicles*, 2021, **10**, e12144.
6. A. Gualerzi, S. Picciolini, C. Carlomagno, F. Rodà and M. Bedoni, *Adv. Drug Deliv. Rev.*, 2021, **174**, 229-249.
7. Y. Yang, C. Zhai, Q. Zeng, A. L. Khan and H. Yu, *Anal. Chem.*, 2020, **92**, 4884-4890.
8. R. P. Carney, R. R. Mizenko, B. T. Bozkurt, N. Lowe, T. Henson, A. Arizzi, A. Wang, C. Tan and S. C. George, *Nat. Nanotechnol.*, 2025, **20**, 14-25.
9. E. Cocucci and J. Meldolesi, *Trends. Cell Biol.*, 2015, **25**, 364-372.
10. S. J. Gould and G. Raposo, *J. Extracell. Vesicles*, 2013, **2**, 20389.

11. F. Qian, Z. Huang, H. Zhong, Q. Lei, Y. Ai, Z. Xie, T. Zhang, B. Jiang, W. Zhu, Y. Sheng, et al., *ACS Nano*, 2022, **16**, 19980-20001.
12. C. Tricarico, J. Clancy and C. D'Souza-Schorey, *Small GTPases*, 2017, **8**, 220-232.
13. L. M. Doyle and M. Z. Wang, *Cells*, 2019, **8**.
14. S. Kaur, F. Livak, G. Daaboul, L. Anderson and D. D. Roberts, *J. Extracell. Vesicles*, 2022, **11**, e12265.
15. B. Ma, L. Li, Y. Bao, L. Yuan, S. Liu, L. Qi, S. Tong, Y. Xiao, L. Qi, X. Fang, et al., *Chem. Biomed. Imaging*, 2024, **2**, 27-46.
16. G. van Niel, D. R. F. Carter, A. Clayton, D. W. Lambert, G. Raposo and P. Vader, *Nat. Rev. Mol. Cell Biol.*, 2022, **23**, 369-382.
17. Y.-J. Liu and C. Wang, *Cell Commun. Signal*, 2023, **21**, 77.
18. Z. Albakova, M. K. S. Siam, P. K. Sacitharan, R. H. Ziganshin, D. Y. Ryazantsev and A. M. Sapozhnikov, *Transl. Oncol.*, 2021, **14**, 100995.
19. M. A. Rogers, F. Buffolo, F. Schlotter, S. K. Atkins, L. H. Lee, A. Halu, M. C. Blaser, E. Tsolaki, H. Higashi, K. Luther, et al., *Sci. Adv.*, 2020, **6**.
20. J. Meldolesi, *Curr. Bio.l*, 2018, **28**, R435-R444.
21. S. Zhang, X. Xiao, Y. Yi, X. Wang, L. Zhu, Y. Shen, D. Lin and C. Wu, *Signal Transduc. Target. Ther.*, 2024, **9**, 149.
22. A. Reale, T. Khong and A. Spencer, *J. Clin. Med.*, 2022, **11**.
23. P. A. Sariano, R. R. Mizenko, V. S. Shirure, A. K. Brandt, B. B. Nguyen, C. Nesiri, B. S. Shergill, T. Brostoff, D. M. Rocke, A. D. Borowsky, et al., *J. Extracell. Vesicles*, 2023, **12**, e12323.
24. K. Al-Nedawi, B. Meehan, J. Micallef, V. Lhotak, L. May, A. Guha and J. Rak, *Nat. Cell Biol.*, 2008, **10**, 619-624.
25. Y. Hui, X. Jiao, L. Yang, D. Lu, Y. Han, W. Yang, Y. Cao, Y. Miao, S. Gong and M. Wei, *Acta Pharm. Sin. B*, 2025, **15**, 3404-3418.
26. W. Tian, N. Lei, J. Zhou, M. Chen, R. Guo, B. Qin, Y. Li and L. Chang, *Cell Death Dis.*, 2022, **13**, 64.
27. M. A. Kumar, S. K. Baba, H. Q. Sadida, S. A. Marzooqi, J. Jerobin, F. H. Altemani, N. Algehainy, M. A. Alanazi, A.-B. Abou-Samra, R. Kumar, et al., *Signal Transduc. Target. Ther.*, 2024, **9**, 27.
28. R. J. Kurman and I.-M. Shih, *Hum. Pathol.*, 2011, **42**, 918-931.
29. K. Guo, Z. Li, A. Win, R. Coreas, G. B. Adkins, X. Cui, D. Yan, M. Cao, S. E. Wang and W. Zhong, *Biosens. Bioelectron.*, 2021, **192**, 113502.
30. S. K. Arya and S. Bhansali, *Chem. Rev.*, 2011, **111**, 6783-6809.
31. L. T. H. Nguyen, J. Zhang, X. Y. Rima, X. Wang, K. J. Kwak, T. Okimoto, J. Amann, M. J. Yoon, T. Shukuya, C. L. Chiang, et al., *J. Extracell. Vesicles*, 2022, **11**, e12258.
32. Y. Tian, L. Ma, M. Gong, G. Su, S. Zhu, W. Zhang, S. Wang, Z. Li, C. Chen, L. Li, et al., *ACS Nano*, 2018, **12**, 671-680.
33. S. Yan, Y. Jiang, C. Liang, M. Cheng, C. Jin, Q. Duan, D. Xu, L. Yang, X. Zhang, B. Ren, et al., *J. Cell. Biochem.*, 2018, **119**, 4113-4119.
34. D. He, H. Wang, S. L. Ho, H. N. Chan, L. Hai, X. He, K. Wang and H. W. Li, *Theranostics*, 2019, **9**, 4494-4507.
35. Z. Li, Y. Y. Ma, J. Wang, X. F. Zeng, R. Li, W. Kang and X. K. Hao, *Onco. Targets Ther.*, 2016, **9**, 139-148.
36. V. Dochez, H. Caillon, E. Vaucel, J. Dimet, N. Winer and G. Ducarme, *J. Ovarian Res.*, 2019, **12**, 28.
37. H. Im, H. Shao, Y. I. Park, V. M. Peterson, C. M. Castro, R. Weissleder and H. Lee, *Nat. Biotechnol.*, 2014, **32**, 490-495.
38. P. Yip, T. H. Chen, P. Seshaiah, L. L. Stephen, K. L. Michael-Ballard, J. P. Mapes, B. C. Mansfield and G. P. Bertenshaw, *PLOS One*, 2011, **6**, e29533.
39. L. T. Brinton, H. S. Sloane, M. Kester and K. A. Kelly, *Cell. Mol. Life Sci.*, 2015, **72**, 659-671.
40. E. Serrano-Pertierra, M. Oliveira-Rodríguez, M. Rivas, P. Oliva, J. Villafani, A. Navarro, M. Blanco-López and E. Cernuda-Morollón, *Bioengineering*, 2019, **6**, 8.
41. R. Linares, S. Tan, C. Gounou and A. R. Brisson, *Methods Mol. Biol.*, 2017, **1545**, 43-54.
42. X. Tan, K. C. Day, X. Li, L. J. Broses, W. Xue, W. Wu, W. Y. Wang, T.-W. Lo, E. Purcell, S. Wang, et al., *Biosens. Bioelectron.: X*, 2021, **8**, 100066.
43. C. V. Raman and K. S. Krishnan, *Nature*, 1928, **121**, 501-502.
44. R. R. Jones, D. C. Hooper, L. Zhang, D. Wolverson and V. K. Valev, *Nanoscale Res. Lett.*, 2019, **14**, 231.
45. R. Pilot, R. Signorini, C. Durante, L. Orian, M. Bhamidipati and L. Fabris, *Biosensors*, 2019, **9**.
46. R. S. Das and Y. K. Agrawal, *Vib. Spectrosc.*, 2011, **57**, 163-176.
47. A. Chandra, V. Kumar, U. C. Garnaik, R. Dada, I. Qamar, V. K. Goel and S. Agarwal, *ACS Omega*, 2024, **9**, 50049-50063.
48. N. U. Huda, R. Z. A. Bari, M. A. Javed, M. N. Kiani and Y. Jin, *Anal. Chem.*, 2026, **98**, 8757-8780.
49. S. Lee, N. A. M. Moussa and S. H. Kang, *Nanomater.*, 2025, **15**, 1153.
50. M. A. Tahir, N. E. Dina, H. Cheng, V. K. Valev and L. Zhang, *Nanoscale*, 2021, **13**, 11593-11634.
51. V. Karunakaran, S. Dadgar, S. K. Paidi, A. F. Mordi, W. A. Lowe, U. M. Mim, J. D. Ivers, J. I. Rodriguez Troncoso, J. A. McPeake, A. Fernandes, et al., *ACS Omega*, 2024, **9**, 43025-43033.
52. S. Kim, T. G. Kim, S. H. Lee, W. Kim, A. Bang, S. W. Moon, J. Song, J.-H. Shin, J. S. Yu and S. Choi, *ACS Appl. Mater. Interfaces*, 2020, **12**, 7897-7904.
53. D. Mrđenović, W. Ge, N. Kumar and R. Zenobi, *Angew. Chem. Int. Ed. Engl.*, 2022, **61**, e202210288.
54. E. Gormally, P. Hainaut, E. Caboux, L. Airoldi, H. Autrup, C. Malaveille, A. Dunning, S. Garte, G. Matullo, K. Overvad, et al., *Int. J. Cancer*, 2004, **111**, 746-749.
55. T. Senapati, M. R. Bittermann, R. Nadar, A. van der Meer, B. Kästner, A. G. Denkova and E. Rühl, *Analyst*, 2025, **150**, 3860-3870.
56. A. C. S. Talari, Z. Movasaghi, S. Rehman and I. u. Rehman, *Appl. Spectrosc. Rev.*, 2015, **50**, 46-111.
57. M. Kopec, K. Beton-Mysur, J. Surmacki and H. Abramczyk, *Sci. Rep.*, 2024, **14**, 16626.
58. W. Lee, A. T. M. Lenferink, C. Otto and H. L. Offerhaus, *J. Raman Spectrosc.*, 2020, **51**, 293-300.
59. A. Bonizzi, L. Signati, M. Grimaldi, M. Truffi, F. Piccotti, S. Gagliardi, G. Dotti, S. Mazzucchelli, S. Albasini, R. Cazzola, et al., *Biosens. Bioelectron.*, 2025, **278**, 117287.
60. M. Fleischmann, P. J. Hendra and A. J. McQuillan, *Chem. Phys. Lett.*, 1974, **26**, 163-166.
61. R. Van Duyne and D. Jeanmaire, *J. Electroanal. Chem.*, 1977, **84**, 1-20.
62. M. G. Albrecht and J. A. Creighton, *J. Am. Chem. Soc*, 1977, **99**, 5215-5217.
63. J. R. Lombardi, *Faraday Discuss*, 2017, **205**, 105-120.
64. J. Langer, D. Jimenez de Aberasturi, J. Aizpurua, R. A. Alvarez-Puebla, B. Auguié, J. J. Baumberg, G. C. Bazan, S. E.

J. Bell, A. Boisen, A. G. Brolo, et al., *ACS Nano*, 2020, **14**, 28-117.

65. K. A. Willets and R. P. Van Duyne, *Annu. Rev. Phys. Chem.*, 2007, **58**, 267-297.
66. D. Cialla, A. März, R. Böhme, F. Theil, K. Weber, M. Schmitt and J. Popp, *Anal. Bioanal. Chem.*, 2012, **403**, 27-54.
67. S. McAughtrie, K. Faulds and D. Graham, *J. Photoc. Photobio. C*, 2014, **21**, 40-53.
68. R. Pilot, R. Signorini, C. Durante, L. Orian, M. Bhamidipati and L. Fabris, *Biosensors*, 2019, **9**.
69. P. Rostron, S. Gaber and D. Gaber, *Laser*, 2016, **21**, 24.
70. K. L. Kelly, E. Coronado, L. L. Zhao and G. C. Schatz, *J. Phys. Chem. B*, 2003, **107**, 668-677.
71. J. Bashir, M. K. Masud, A. S. Nugraha, C. H. Liu, A. Vasanth, A. Ashok, S. M. A. Hossain, E. Ahmed, T. Pejovic, T. Morgan, et al., *Small*, 2025, **21**, e2401817.
72. Y. Li, Y. Wang, J. Tian and J. A. Huang, *Methods Mol. Biol.*, 2023, **2668**, 15-22.
73. Y. Xie, X. Su, Y. Wen, C. Zheng and M. Li, *Nano. Lett.*, 2022, **22**, 7910-7918.
74. H. Shin, B. H. Choi, O. Shim, J. Kim, Y. Park, S. K. Cho, H. K. Kim and Y. Choi, *Nat. Commun.*, 2023, **14**, 1644.
75. K. H. W. Ho, H. Lai, R. Zhang, H. Chen, W. Yin, X. Yan, S. Xiao, C. Y. K. Lam, Y. Gu, J. Yan, et al., *ACS Sens.*, 2024, **9**, 4860-4869.
76. C. Hong, S. Yang and J. C. Ndukaife, *Nanoscale Adv.*, 2023, **5**, 2973-2978.
77. X. Luo, Y. Xing, D. D. Galvan, E. Zheng, P. Wu, C. Cai and Q. Yu, *ACS Sens.*, 2019, **4**, 1534-1542.
78. L. Ngo, W. Zhang, S. S. T. Hnit and Y. Wang, *Analyst*, 2023, **148**, 3074-3086.
79. C.-F. Ning, L. Wang, Y.-F. Tian, B.-C. Yin and B.-C. Ye, *Analyst*, 2020, **145**, 2795-2804.
80. Q. Zhang, R. Ma, Y. Zhang, J. Zhao, Y. Wang and Z. Xu, *ACS Sens.*, 2023, **8**, 875-883.
81. S. Dong, Y. Wang, Z. Liu, W. Zhang, K. Yi, X. Zhang, X. Zhang, C. Jiang, S. Yang, F. Wang, et al., *ACS Appl. Mater. Interfaces*, 2020, **12**, 5136-5146.
82. M. Jalali, I. Isaac Hosseini, T. AbdelFatah, L. Montermini, S. Wachsmann Hogiu, J. Rak and S. Mahshid, *Lab Chip*, 2021, **21**, 855-866.
83. P. A. Mosier-Boss, *Nanomater*, 2017, **7**, 142.
84. J. Wang, K. M. Koo, Y. Wang and M. Trau, *Adv. Sci.*, 2019, **6**, 1900730.
85. Y. Chen, *Microelectron. Eng.*, 2015, **135**, 57-72.
86. F. Watt, A. A. Bettiol, J. A. Van Kan, E. J. Teo and M. B. H. Breese, *Int. J. Nanosci.*, 2005, **04**, 269-286.
87. M. Jalali, C. del Real Mata, L. Montermini, O. Jeanne, I. I.Hosseini, Z. Gu, C. Spinelli, Y. Lu, N. Tawil, M. C. Guiot, et al., *ACS Nano*, 2023, **17**, 12052-12071.
88. N. M. Ćulum, T. T. Cooper, G. I. Bell, D. A. Hess and F. Lagugné-Labarthet, *Anal. Bioanal. Chem.*, 2021, **413**, 5013-5024.
89. N. M. Ćulum, T. T. Cooper, G. A. Lajoie, T. Dayarathna, S. H. Pasternak, J. Liu, Y. Fu, L.-M. Postovit and F. Lagugné-Labarthet, *Analyst*, 2021, **146**, 7194-7206.
90. P. Verma, *Chem. Rev*, 2017, **117**, 6447-6466.
91. T. Itoh, M. Procházka, Z.-C. Dong, W. Ji, Y. S. Yamamoto, Y. Zhang and Y. Ozaki, *Chem. Rev.*, 2023, **123**, 1552-1634.
92. J. Wessel, *J. Opt. Soc. Am. B*, 1985, **2**, 1538-1541.
93. R. M. Stöckle, Y. D. Suh, V. Deckert and R. Zenobi, *Chem. Phys. Lett.*, 2000, **318**, 131-136.
94. N. Hayazawa, Y. Inouye, Z. Sekkat and S. Kawata, *Opt. Commun.*, 2000, **183**, 333-336.
95. M. S. Anderson, *Appl. Phys. Lett*, 2000, **76**, 3130-3132.
96. B. Pettinger, G. Picardi, R. Schuster and G. Ertl, *Electrochem.*, 2000, **68**, 942-949.
97. N. Kazemi-Zanjani, S. Vedraine and F. Lagugné-Labarthet, *Opt. Express*, 2013, **21**, 25271-25276.
98. T. Deckert-Gaudig and V. Deckert, *Small*, 2009, **5**, 432-436.
99. F. Pashaee, R. Hou, P. Gobbo, M. S. Workentin and F. Lagugné-Labarthet, *J. Phys. Chem. C*, 2013, **117**, 15639-15646.
100. D. Mrđenović, W. Ge, N. Kumar and R. Zenobi, *Angew. Chem. Int. Ed.*, 2022, **61**, e202210288.
101. L. Buccini, A. Proietti, G. La Penna, C. Mancini, F. Mura, S. Tacconi, L. Dini, M. Rossi and D. Passeri, *Nanoscale*, 2024, **16**, 8132-8142.
102. T. Stepanenko, K. Sofińska, N. Wilkosz, J. Dybas, E. Wiercigroch, K. Bulat, E. Szczesny-Malysiak, K. Skirlińska-Nosek, S. Seweryn, J. Chwiej, et al., *Analyst*, 2024, **149**, 778-788.
103. L. Veliz, C. Lambin, T. T. Cooper, W. M. McCarvell, G. A. Lajoie, L.-M. Postovit and F. Lagugné-Labarthet, *Nanoscale*, 2025, **17**, 9926-9936.
104. S. Srivastava, W. Wang, W. Zhou, M. Jin and P. J. Vikesland, *Environ. Sci. Technol.*, 2024, **58**, 20830-20848.
105. M. Ringnér, *Nat. Biotechnol.*, 2008, **26**, 303-304.
106. H. J. Koster, T. Rojalin, A. Powell, D. Pham, R. R. Mizenko, A. C. Birkeland and R. P. Carney, *Nanoscale*, 2021, **13**, 14760-14776.
107. M. Imanbekova, S. Suarasan, T. Rojalin, R. R. Mizenko, S. Hilt, M. Mathur, P. Lepine, M. Nicouleau, N.-V. Mohamed, T. M. Durcan, et al., *Nanoscale Adv*, 2021, **3**, 4119-4132.
108. G. Li, N. Zhu, J. Zhou, K. Kang, X. Zhou, B. Ying, Q. Yi and Y. Wu, *J. Mater. Chem. B*, 2021, **9**, 2709-2716.
109. M. Russo, L. Tirinato, F. Scionti, M. L. Coluccio, G. Perozziello, C. Riillo, V. Mollace, S. Gratteri, N. Malara, M. T. Di Martino, et al., *ACS Omega*, 2020, **5**, 30436-30443.
110. C. del Real Mata, Y. Lu, M. Jalali, A. Bocan, M. Khatami, L. Montermini, J. McCormack-Ilersich, W. W. Reisner, L. Garzia, J. Rak, et al., *Sens. Diagn*, 2025, **4**, 869-883.
111. X. Diao, X. Li, S. Hou, H. Li, G. Qi and Y. Jin, *Anal. Chem.*, 2023, **95**, 7552-7559.
112. L. Veliz, T. T. Cooper, I. Grenier-Pleau, S. A. Abraham, J. Gomes, S. H. Pasternak, B. Dauber, L. M. Postovit, G. A. Lajoie and F. Lagugné-Labarthet, *ACS Sens.*, 2024, **9**, 272-282.
113. A. Nakar, Z. e. Schmilovitch, D. Vaizel-Ohayon, Y. Kroupitski, M. Borisover and S. Sela, *Water Res.*, 2020, **169**, 115197.
114. Y. Hernández, L. K. Lagos and B. C. Galarreta, *Sens. Bio-Sens. Res.*, 2020, **28**, 100331.
115. C. Wang, Y. Long, W. Li, W. Dai, S. Xie, Y. Liu, Y. Zhang, M. Liu, Y. Tian, Q. Li, et al., *Sci. Rep*, 2020, **10**, 5880.
116. S. Seifert, *Sci. Rep.*, 2020, **10**, 5436.
117. G. Pyrgiotakis, O. E. Kundakcioglu, P. M. Pardalos and B. M. Moudgil, *J. Raman Spectrosc.*, 2011, **42**, 1222-1231.
118. Q. He, H. J. Koster, J. O'Sullivan, S. G. Ono, H. J. O'Toole, G. S. Leiserowitz, M. C. Heffern and R. P. Carney, *Biosens. Bioelectron.*, 2025, **288**, 117800.
119. X. Xie, W. Yu, Z. Chen, L. Wang, J. Yang, S. Liu, L. Li, Y. Li and Y. Huang, *Nanoscale*, 2023, **15**, 13466-13472.

View Article Online
DOI: 10.1039/D6AN00476H

120. J. Q. Li, P. V. Dukes, W. Lee, M. Sarkis and T. Vo-Dinh, *J. Raman Spectrosc.*, 2022, **53**, 2044-2057.
121. H. Chen, L. Wang, D. Fan, P. Ma, X. Zhang and K. Lin, *Analyst*, 2025, **150**, 4332-4341.
122. M. Chen, H. Wang, Y. Zhang, H. Jiang, T. Li, L. Liu and Y. Zhao, *Anal. Chem.*, 2024, **96**, 6794-6801.
123. A. Dazzi, R. Prazeres, F. Glotin and J. M. Ortega, *Infrared Phys. Technol.*, 2006, **49**, 113-121.
124. D. Khanal, A. Kondyurin, H. Hau, J. C. Knowles, O. Levinson, I. Ramzan, D. Fu, C. Marcott and W. Chrzanowski, *Anal. Chem.*, 2016, **88**, 7530-7538.
125. T. Dou, Z. Li, J. Zhang, A. Evilevitch and D. Kurouski, *Anal. Chem.*, 2020, **92**, 11297-11304.
126. S. Rizevsky and D. Kurouski, *ChemBioChem*, 2020, **21**, 481-485.
127. M. S. Ural, E. Dartois, J. Mathurin, D. Desmaële, P. Collery, A. Dazzi, A. Deniset-Besseau and R. Gref, *Analyst*, 2022, **147**, 5564-5578.
128. N. Hondl, L. Neubauer, V. Ramos-Garcia, J. Kuligowski, M. Bishara, E. Sevcsik, B. Lendl and G. Ramer, *ACS Meas. Sci. Au*, 2025, **5**, 469-476.
129. S. Y. Kim, D. Khanal, P. Tharkar, B. Kalionis and W. Chrzanowski, *Nanoscale Horiz.*, 2018, **3**, 430-438.
130. S. C. Terry, J. H. Jerman and J. B. Angell, *IEEE Trans. Electron. Devices*, 1979, **26**, 1880-1886.
131. S. Lian, X. Li and X. Lv, *ACS Appl. Mater. Interfaces*, 2025, **17**, 10193-10230.
132. A. Gharatape, Z. Niasari-Naslaji, J. Leblond Chain, N. Tabatabaei and R. Faridi-Majidi, *Nanoscale*, 2025, **17**, 23822-23853.
133. F. S. N. Lye, Y. S. Loo, I. D. Mat Azmi, C. S. Lee, N. I. Zahid and T. Madheswaran, *Microfluid. Nanofluid*, 2025, **29**, 51.
134. K. B. Shanmugasundaram, J. Li, A. I. Sina, A. Wuethrich and M. Trau, *Mater. Adv.*, 2022, **3**, 1459-1471.
135. L. Wu, X. Liu, Y. Zhang, Z. Yang, L. Chen, S. Zong, J. Li, Y. Cui and Z. Wang, *Sens. Actuators B Chem.*, 2024, **401**, 135081.
136. H. Chen, H. Liu, L. Xing, D. Fan, N. Chen, P. Ma and X. Zhang, *ACS Sens.*, 2025, **10**, 2872-2882.

View Article Online
DOI: 10.1039/D6AN00476H

Data Availability Statement

This manuscript is a mini review and therefore do not contain original data that have not been published elsewhere.

All authorizations for use of some figures (x9) were obtained from the journals, Creative Commons and Copyright clearance center depending on the manuscript.